Joint Synoptic and Cloud Variability over the Northeast Atlantic near the Azores

DAVID B. MECHEM AND CARLY S. WITTMAN

Department of Geography and Atmospheric Science, University of Kansas, Lawrence, Kansas

MATTHEW A. MILLER AND SANDRA E. YUTER

Department of Marine, Earth, and Atmospheric Sciences, North Carolina State University, Raleigh, North Carolina

SIMON P. DE SZOEKE

College of Oceanic and Atmospheric Sciences, Oregon State University, Corvallis, Oregon

(Manuscript received 26 July 2017, in final form 26 January 2018)

ABSTRACT

Marine boundary layer clouds are modified by processes at different spatial and temporal scales. To isolate the processes governing aerosol–cloud–precipitation interactions, multiday synoptic variability of the environment must be accounted for. Information on the location of low clouds relative to the ridge–trough pattern gives insight into how cloud properties vary as a function of environmental subsidence and stability. The technique of self-organizing maps (SOMs) is employed to objectively classify the 500-hPa geopotential height patterns for 33 years of reanalysis fields (ERA-Interim) into pretrough, trough, posttrough, ridge, and zonal-flow categories. The SOM technique is applied to a region of prevalent marine low cloudiness over the eastern North Atlantic Ocean that is centered on the Azores island chain, the location of a long-term U.S. Department of Energy observation site. The Azores consistently lie in an area of substantial variability in synoptic configuration, thermodynamic environment, and cloud properties. The SOM method was run in two ways to emphasize multiday and seasonal variability separately. Over and near the Azores, there is an east-to-west sloshing back and forth of the western edge of marine low clouds associated with different synoptic states. The different synoptic states also exhibit substantial north–south variability in the position of high clouds. For any given month of the year, there is large year-to-year variability in the occurrence of different synoptic states. Hence, estimating the climatological behavior of clouds from short-term field campaigns has large uncertainties. This SOM approach is a robust method that is broadly applicable to characterizing synoptic regimes for any location.

1. Introduction

Observations of marine boundary layer (MBL) clouds show that they are highly variable over a wide range of spatial and temporal scales (Klein et al. 1995; Klein 1997; Caldwell et al. 2005; Stevens et al. 2005; Wood and Hartmann 2006; Burleyson et al. 2013; de Szoeke et al. 2016). Untangling the relative sensitivity of low-cloud fraction to aerosol–cloud–precipitation interactions as a function of synoptic-scale[1] (characteristic length scale L of approximately 1000 km) changes in the environment requires quantification of the environmental context (e.g., Coopman et al. 2016). Information on where the low clouds are located relative to the ridge–trough pattern gives insight into how cloud properties vary as a function of environmental subsidence, advection, and stability.

Supplemental information related to this paper is available at the Journals Online website: https://doi.org/10.1175/JAMC-D-17-0211.s1.

Corresponding author: David B. Mechem, dmechem@ku.edu

[1] For the purposes of this paper, we use the terms synoptic scale and large scale synonymously, since baroclinic synoptic-scale waves are embedded in a slowly varying large-scale flow and the synoptic-scale low pressure systems preferentially form in large-scale trough regions.

DOI: 10.1175/JAMC-D-17-0211.1

Low clouds are frequently found within synoptic waves at locations corresponding to several distinct well-known associations between clouds and atmospheric circulation patterns (Lau and Crane 1995, 1997). MBL stratocumulus, for example, can exist under a number of different synoptic configurations. Stratocumulus often occur east of the midtropospheric ridge axis, where the presence of a subtropical high is associated with large-scale subsidence (Norris 1998; Norris and Klein 2000). Stratocumulus are also frequently found behind the surface trough, in the region of cold-air advection (Mechem et al. 2010). Stratocumulus and optically thick stratus can also be present in the cyclone warm sector (Lau and Crane 1997).

The Azores islands in the northeastern Atlantic Ocean have served as a site for several field campaigns to study low-cloud transitions. The Atlantic Stratocumulus Transition Experiment (ASTEX; Albrecht et al. 1995) in June of 1992 used a combination of island, aircraft, ship, and satellite measurements to study the transition from stratocumulus to trade cumulus. Substantial variations in cloud properties were found between clean marine air masses and more-polluted air masses of continental origin. In the summer, the environment near the Azores is dominated by the subtropical Bermuda high pressure center (Hasanean 2004; Li et al. 2011). In addition, weak synoptic influence from cyclones to the north of the Azores affects the prevailing wind direction and hence airmass origin. The 18-month Clouds, Aerosol, and Precipitation in the Marine Boundary Layer project (CAP-MBL; Wood et al. 2015) centered on Graciosa Island (39.09°N, 28.03°W; 15.24-m altitude) examined the interactions among clouds, aerosol, and precipitation throughout the year. Rémillard et al. (2012) found that low clouds were the dominant cloud type (present 40%–60% of the time) year-round with the highest frequencies of occurrence in summer and autumn. Multiyear observations of clouds from Graciosa Island are currently being made as part of the U.S. Department of Energy's Atmospheric Radiation Measurement Program Eastern North Atlantic (ENA) fixed site (https://www.arm.gov/capabilities/observatories/ena).

Accounting for environmental context helps to disentangle the roles of physical mechanisms that may be simultaneously active in low-cloud systems. For example, Myers and Norris (2013) used satellite data and reanalysis at seasonal time scales to examine variations in cloud properties as a function of subsidence and inversion strength. Their results yielded important new insights on climate sensitivity of low clouds to stronger inversions and weaker subsidence. This paper follows the philosophy of Myers and Norris (2013) by setting the stage for examination of the most relevant physical mechanisms underlying the observed *multiday* variability of low-cloud fields near the Azores. To this end, we characterize the synoptic state in an objective and unsupervised manner using the approach of self-organizing maps (SOMs). The SOM method applied to the 500-hPa geopotential height field from reanalysis is combined with cloud information from satellite observations and additional quantities from reanalysis to document the dominant synoptic states and their characteristic cloud properties. We classify on the basis of synoptic state and then examine cloud properties associated with each synoptic state, since we are interested in attributing behaviors of cloud properties to specific forcings. The approach of classifying on the basis of cloud properties and then examining the meteorological conditions (e.g., Rémillard and Tselioudis 2015) permits the possibility that the same cloud type can occur in very different synoptic states, which makes attribution to specific physical forcing mechanisms ambiguous. A broader aim for our study is to advocate for the SOM approach as a robust and broadly applicable method to characterize synoptic regimes for any given location.

2. Methods and data

a. *Approaches to synoptic classification*

A number of synoptic classification techniques exist, each with inherent assumptions and advantages, but all with the overarching goal of characterizing different phases of the synoptic-scale wave pattern into classes and the relation of atmospheric properties to each class (Hewitson and Crane 2002). The concept of synoptic classification extends as far back as the late nineteenth century (Köppen 1874; Abercromby 1883), and early synoptic classifications (also termed synoptic typing) were done manually (e.g., Lamb 1950). Although this method was effective, it was labor intensive.

A number of automated approaches have been developed to alleviate the labor-intensive nature of synoptic typing, chief among them linear decomposition methods like empirical orthogonal functions (EOFs), k-means clustering, and self-organizing maps. The approach of SOMs is an automated neural-network technique that produces a user-defined number of data states (synoptic regimes, in our case), continuously distributed and spanning the parameter space of the data (Hewitson and Crane 1992; Kohonen 2001). SOMs have been employed for synoptic and climate classification (Cavazos 2000; Reusch et al. 2007; Bailey et al. 2011; Kennedy et al. 2016), cloud classification (Ambroise et al. 2000), and extreme weather (Cassano et al. 2006). The SOM analysis produces a continuous distribution of synoptic regimes ranging from trough to ridge (Hewitson and Crane 2002). Decomposing synoptic patterns into a continuum of regimes using SOMs has an advantage over linear methods like EOF decomposition, which produces orthogonal basis functions in space (EOFs) that may or may not bear any resemblance to actual physical structures.

All synoptic classification approaches share a common goal of maximizing within-group similarity while minimizing between group similarity (Balling 1984). SOMs are similar to other traditional forms of cluster analysis, such as *k*-means clustering, in which nodes are distributed within a cloud of data, assigning more nodes in regions of higher densities of data. The main difference between SOMs and *k*-means clustering lies in the primary goal of the SOM, which is to create a continuum of nodes that cumulatively represent the multidimensional distribution of the entire dataset rather than simply representing individual clusters of data. Because of the neighborhood function, the continuum of nodes produced by the SOM method may sacrifice some exactness relative to a *k*-means clustering approach.

The SOM procedure is characterized by a competitive learning process that directs input data to its best matching (“winning”) node. As the competitive learning process takes place, nodes surrounding the winning node (“neighborhood” nodes) adjust toward the winner. This learning stage employs a neighborhood function to update not only the winning node but also the surrounding nodes as well. This neighborhood function is what distinguishes SOMs from a *k*-means clustering approach. The competitive learning and adjustment of the nodes is self-defined on the basis of the data alone and is not dictated by preconceptions of how the synoptic patterns should be distributed. Thus, the SOM analysis constitutes an unsupervised learning process, ultimately resulting in an objective classification of synoptic states.

b. Data

The SOM calculations are based on reanalysis fields from ERA-Interim (ERA-I; Dee et al. 2011) from the Computational and Information Systems Laboratory Research Data Archive (managed by the National Center for Atmospheric Research with data from ERA-I products; http://rda.ucar.edu/). The 6-hourly reanalysis products lie on a 0.7° × 0.7° grid and span the period from January 1979 to October 2012. The analysis employs geopotential height and vertical velocity at the 1000-, 850-, 700-, and 500-hPa pressure levels. Cloud fraction, temperature, and cloud liquid- and ice-water mixing ratios (condensate) are obtained for all available pressure levels. The SOM nodes are determined strictly from the 500-hPa geopotential height fields.

The stability of the MBL inversion is quantified using estimated inversion strength (EIS; Wood and Bretherton 2006):

$$\mathrm{EIS} = (\theta_{700} - \theta_{\mathrm{surface}}) - \Gamma_m^{850}(z_{700} - \mathrm{LCL}), \qquad (1)$$

where Γ_m^{850} is the moist-adiabatic lapse rate at the 850-hPa pressure level, LCL is the height of the lifting condensation level, z_{700} is the height of the 700-hPa pressure level, and θ_{700} and $\theta_{\mathrm{surface}}$ are the potential temperatures of the 700-hPa level and surface, respectively. We note that the reanalysis products can sometimes struggle to represent the boundary layer. For example, Dee et al. (2011) found that the surface energy balance in ERA-I is poor, related to a bias in downwelling solar radiation, which we surmise is due to the representation of low clouds. Seidel et al. (2012) and Jakobson et al. (2012) similarly find reanalysis products lacking in various ways when validated against independent observations of boundary layer properties. It is difficult to know how well the ERA-I performs over the ENA site, although our limited comparison of ERA-I and observed values of lower-tropospheric stability during the CAP-MBL campaign (not shown) suggests that ERA-I is sufficient at least for assessing relative differences in stability across the SOM nodes.

Projections of MODIS and ERA-I cloud fraction onto the SOM nodes illustrate the mean spatial distribution of cloud cover for each node. We also examine cloud-top temperature and total condensate as complementary measures of cloud properties. Cloud fraction profiles from the reanalysis pressure levels are employed to calculate the total cloud fraction using the standard maximum/random overlap assumption [Eq. (4) in Oreopoulos and Khairoutdinov (2003)].

Cloud-top temperature (CTT) in the reanalysis is calculated using the highest point at which cloud is present, using liquid- and ice-water-content thresholds. Given the discrete nature of the pressure levels in the dataset, the actual highest point of cloud may be underestimated somewhat, and therefore CTT may be overestimated (too warm). We found that the CTT calculation was not particularly sensitive to threshold values of liquid or ice water content. For the reanalysis vertical grid and a standard atmospheric lapse rate of 6.5 K km^{-1}, a one-gridpoint uncertainty in classifying cloud top yields CTT uncertainty estimates of at most 1.5 K at 900 hPa and 4.8 K at 500 hPa.

Moderate Resolution Imaging Spectroradiometer (MODIS) retrievals (Platnick et al. 2003) from the *Aqua* satellite (approximately 0130 and 1330 local time overpasses) supply the primary measures of cloud properties over the ENA site. These data span the period from

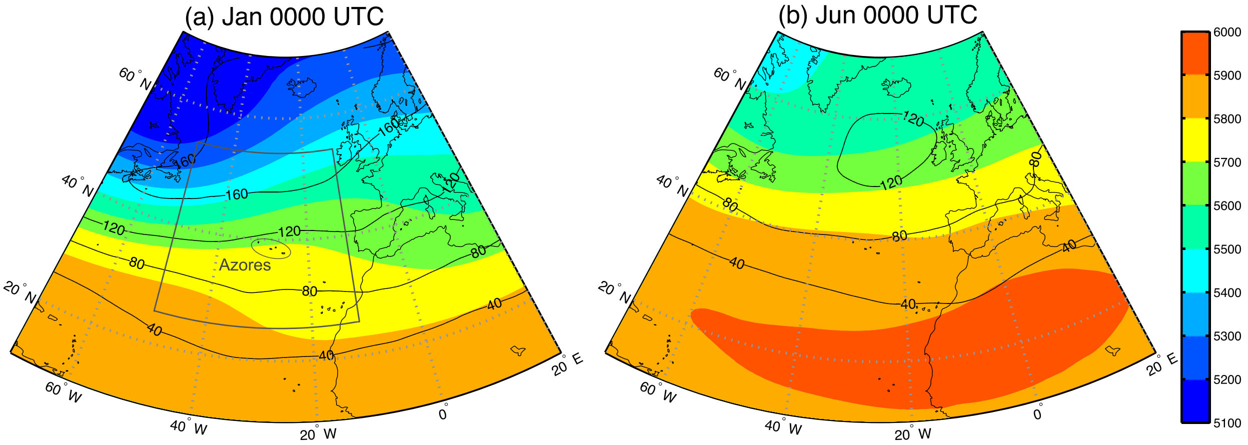

FIG. 1. Mean 500-hPa heights (color shading) for (a) January and (b) June. The inner box in (a) represents the smaller domain used to explore variability in the vicinity of the Azores. Black contour lines are standard deviation of the mean 500-hPa height and can be used as a proxy for storm-track variability, with larger numbers indicating greater variability.

2002 to 2012 and are used in conjunction with the reanalysis. Although nighttime *Terra* retrievals (2230 LT) are closer in time to the 0000 UTC ERA-I data used, nighttime *Aqua* retrievals (0130 LT) are used because of a spurious, persistent, cone-shaped artifact in the *Terra* cloud-fraction products. MODIS cloud-fraction properties come from the "MYD08_L3" daily global product available on a 1° × 1° equal-area grid (https://modis-atmosphere.gsfc.nasa.gov/MOD08_D3/index.html). Comparison of MODIS cloud retrievals with cloud properties calculated from reanalysis is not trivial, largely because of the possibility of overlapped clouds. The presence of high cloud will mask low cloud and cause a systematic underestimate of low/liquid cloud fraction. To sidestep this difficulty, we examine MODIS estimates of total cloud fraction and cloud-top temperature (which we take as a measure of the highest layer) from the MYD08_L3 "Cloud_Mask_5km" MODIS product.

c. *Self-organizing maps*

Following the approach of Hewitson and Crane (2002), we employ the technique of self-organizing maps to classify synoptic regime. Although some studies base their synoptic regime classification on surface pressure or 1000-hPa geopotential heights (Hewitson and Crane 2002), we select the 500-hPa level because the overwhelming dominance of the Bermuda high (particularly during the summer months) renders the 1000-hPa height field a poor discriminator of synoptic regime. Furthermore, the 500-hPa level plays a central role in governing midlatitude dynamics.

The analysis domain is a grid of 42 points (latitude) × 57 points (longitude), covering the outlined area in Fig. 1a and lying between approximately 25° and 55°N and between 50° and 10°W. This area is roughly centered on Graciosa Island, which is the site of the CAP-MBL field campaign (Wood et al. 2015). A number of sensitivity tests established this domain as the best analysis domain for our purposes. Smaller areas were not big enough to represent synoptic wave structure; larger areas tended to overly emphasize prominent climatological structures (particularly the Icelandic low), which then dominated the regime classification. We run the SOM algorithm on each month, and we choose to highlight January and June because of their significance to the annual cloud cycle.

When raw 500-hPa heights were used in early tests of our SOM analysis, variability over northern latitudes exerted undue influence on the synoptic classification. For this reason, we instead employ normalized anomalies of the 500-hPa height field, calculated over the 33-yr span of the reanalysis dataset:

$$\langle Z\rangle = \frac{Z-\overline{Z}}{\sigma_Z}\cos\phi, \qquad (2)$$

where Z is the 500-hPa geopotential height, $\overline{Z}$ is a mean 500-hPa height calculated over some time interval, σ_Z is the standard deviation calculated over that same interval, and ϕ is latitude. An equal-area assumption is applied ($\cos\phi$) to avoid unduly weighting the polar regions (Gong and Wang 1999).

Anomalies are calculated using either monthly averaging windows or a window that is the length of the entire reanalysis dataset available at the time. For the month-by-month classifications, the normalization is calculated by subtracting a 31-day centered, running mean (±15 days) from each data sample and then

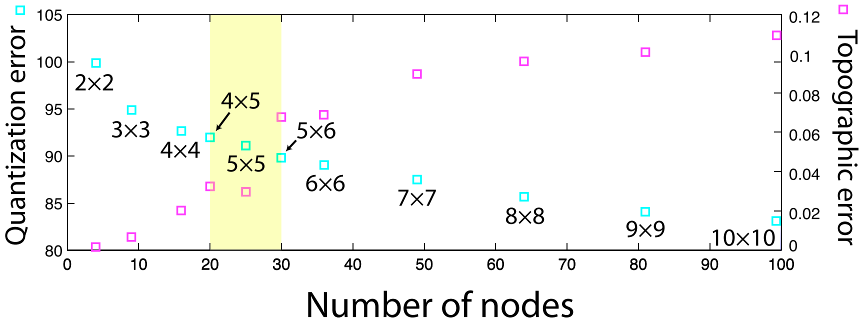

Fig. 2. Elbow plot used to evaluate the optimal number of nodes. Quantization error (m) decreases with an increasing number of nodes while topographic error increases with an increasing number of nodes. The optimal number chosen is 25 nodes, highlighted in the region shaded with yellow. Note that the nonsquare map orientations are wider than they are tall.

dividing that sample for a given day by the standard deviation of that 31-day window. Calculating anomalies on the basis of monthly mean and standard deviation is in effect a high-pass filter that removes variability at monthly periods and longer, leaving the multiday (synoptic) variability untouched. Running the SOM analysis on the monthly-window anomalies emphasizes multiday synoptic variability, which can include, for example, intrusions of weak troughs into the Azores region during the summer when the Bermuda high is dominant. Using the monthly-window anomalies also has the advantage of alleviating concerns of possible seasonal biases in the reanalysis (e.g., Kennedy et al. 2011; Betts and Beljaars 2017). Running the SOM analysis on anomalies that are based on a mean and standard deviation taken from the entire length of the reanalysis, on the other hand, emphasizes the seasonal cycle.

All of our SOM analyses used the "MATLAB" software SOM toolbox (SOM_PAK; http://www.cis.hut.fi/projects/somtoolbox). The SOM is applied to the normalized anomalies for 500-hPa geopotential heights at 0000 UTC. We find that a once-daily snapshot of the synoptic state at 0000 UTC is sufficient for characterizing the synoptic classification. Furthermore, the classification is insensitive to the choice of specific time; the classification that is based on 1800 UTC reanalysis, for example, varies little from that for 0000 UTC. After the nodes are constructed, each 500-hPa synoptic state is mapped to a node that best resembles its configuration by minimizing a Euclidean distance between the two. Each SOM node is therefore associated with a set of dates that are uniquely mapped to that particular node.

d. *Choice of number of nodes*

The number of nodes is an important user-defined parameter. To represent the full continuum of synoptic behavior for over 30 years of data, it is imperative to choose a sufficient number of nodes. Using too few nodes overgeneralizes the data and potentially combines distinct states into too few categories; use of too many nodes, on the other hand, creates an overwhelming number of synoptic states to decipher, with similar synoptic states spread across multiple nodes. One way to identify an optimal number of nodes is to run the SOM algorithm across a range of different map sizes (from 2 × 2 to 10 × 10) and then evaluate different SOM error metrics.

We evaluated two error metrics across a number of map-size configurations, and the number of nodes is determined by subjective competing constraints represented by these two error metrics. Following the concept of the elbow criterion (Tibshirani et al. 2001), we calculate the quantization error (a measure of intranode variability computed as the average Euclidean distance between the data and its classified node) across the range of map sizes. The elbow criterion describes the point at which the addition of nodes "fail[s] to add a significant amount of information" (Schuenemann et al. 2009) to the SOM, justifying the lower bound for the number of nodes necessary to represent the input data. The topographic error (the proportion of all data samples for which the best-matched node and the second-best-matched node are not adjacent in the node map; Kohonen 2001) generally behaves in a manner opposite to that of the quantization error, increasing with the number of nodes as successive time levels of data become more likely to be mapped to nonadjacent nodes. The point at which adding nodes drastically increases the topographic error constitutes an upper bound for the ideal SOM size. Our tests over this analysis region suggest that a map size of 25 nodes (5 × 5) is optimal for this study (see Fig. 2). Although the SOM documentation recommends the use of nonsquare map sizes for a more stable learning process (Kohonen et al. 1996), our tests summarized in Fig. 2 include examples of both square and slightly nonsquare map sizes. We are not able to distinguish a substantial difference in training behavior between the two. In the interests of replicability, using the MATLAB SOM_PAK routine, the function call to compute all of our SOM maps is ‘‘sm0 = som_make (geo, ’rect’, ’msize’, [5 5]);.’’

e. Projections of environmental and cloud properties

At its core, the SOM analysis represents the mapping of each data point (specific dates, in our case) to a node. Once the SOM procedure determines the nodes, in principle any data source inside the date range used to construct the nodes can be composited (mapped) into node space. We refer to this process as ‘‘compositing’’ or ‘‘projecting’’ variables onto the nodes, acknowledging that this use of the term projecting differs from standard EOF usage in which data are projected onto orthogonal basis structures. The projections of other atmospheric variables from the reanalysis onto the SOM nodes more completely describes the synoptic configuration.

We project a number of variables onto the SOM nodes, both from reanalysis and from MODIS retrievals: 1000-hPa geopotential heights, ERA-I and MODIS total cloud fraction and cloud-top temperature, total condensate (the sum of liquid and ice water contents), EIS, and vertical velocity. It is important to note that these projected variables have no influence on the actual SOM analysis itself (i.e., how the nodes are determined), which employs only the normalized 500-hPa geopotential height anomaly field.

3. Example of dominant synoptic configurations—June

Figure 1 shows the mean 500-hPa height structure for January and June. Our analysis includes all months, but our discussion emphasizes June and January, since those months exhibit maxima in both total cloud fraction and low-cloud fraction (Rémillard et al. 2012). The SOM nodes (numbered according to matrix notation) calculated for June are presented in Fig. 3 as the positive (solid lines) and negative (dashed lines) mean monthly-window anomalies for the data times mapped to each specific node. Shown with the anomalies are the mean 500-hPa geopotential heights (color shading) projected on each node. The SOM node space spans a continuum of anomalies ranging from almost entirely positive values (node 35), through one-half positive and one-half negative (nodes 53 and 13), to nearly all negative (node 31). The relative-frequency values for each node (Fig. 3) indicate that these archetypal nodes tend to exhibit the highest frequencies among all the nodes. The highest-frequency nodes need not be on the midpoints along each edge but more generally lie on the outside perimeter of the node configuration. The middle node (33) is characterized by a nearly uniform zero anomaly and may be interpreted as being close to the climatological mean.

Means of the 500-hPa geopotential heights from the dates associated with each node promote a meteorological interpretation of the SOM nodes. Positive anomaly structures correspond to heights greater than the climatological mean but not necessarily to a ridgelike structure. In a similar way, negative anomalies do not necessarily correspond to a trough. Note that the near-zero anomaly state (node 33) corresponds to a structure that is slightly perturbed from simple zonal flow, with the Azores lying just east of a weak ridge axis and just barely west of a weak trough axis. Nodes 35 and 31 are characterized by ridge and trough axes, respectively, centered over the Azores. The Azores lie in a region of strong 500-hPa geopotential height gradients in two other very frequent nodes (53 and 13). We denote these nodes as archetypal ‘‘pretrough’’ (node 53) and ‘‘posttrough’’ (node 13) patterns determined by the location of the trough axis relative to the Azores. Although the geopotential heights over the analysis domain rarely drop below 5400 m in June, the Azores regularly experience the influence of synoptic activity (e.g., nodes 41, 31, and 21). These nodes represent an intrusion of synoptic low pressure systems over the Azores.

On the basis of the position of the 500-hPa ridge and trough axes relative to the Azores, for each month we further cluster each node into different synoptic categories. Although objective methods for classifying SOM nodes exist (e.g., Vesanto and Alhoniemi 2000), we classify the 25 nodes by hand from the 500-hPa geopotential heights and anomalies, using our understanding of the structure of midlatitude synoptic systems. In addition, some months contain ‘‘unclassified’’ nodes. The most extreme or high-frequency nodes are easiest to classify. Nodes that are more difficult to classify, for example at the transition of different classes, typically have fewer data times mapped to them (i.e., lower frequency) such that these difficult-to-classify nodes will have little impact on the frequency of the different classes. Figures S1–S12 in the online supplemental material to this paper show the SOM nodes and synoptic category breakdown for all 12 months.

4. Annual cycle in synoptic regimes

We characterize the annual cycle of synoptic regimes by applying the SOM analysis to the monthly-window anomalies (calculated using the centered/running mean and standard deviation) for each month calculated as described above and then classifying the nodes into pretrough, trough, posttrough, ridge, or zonal categories.

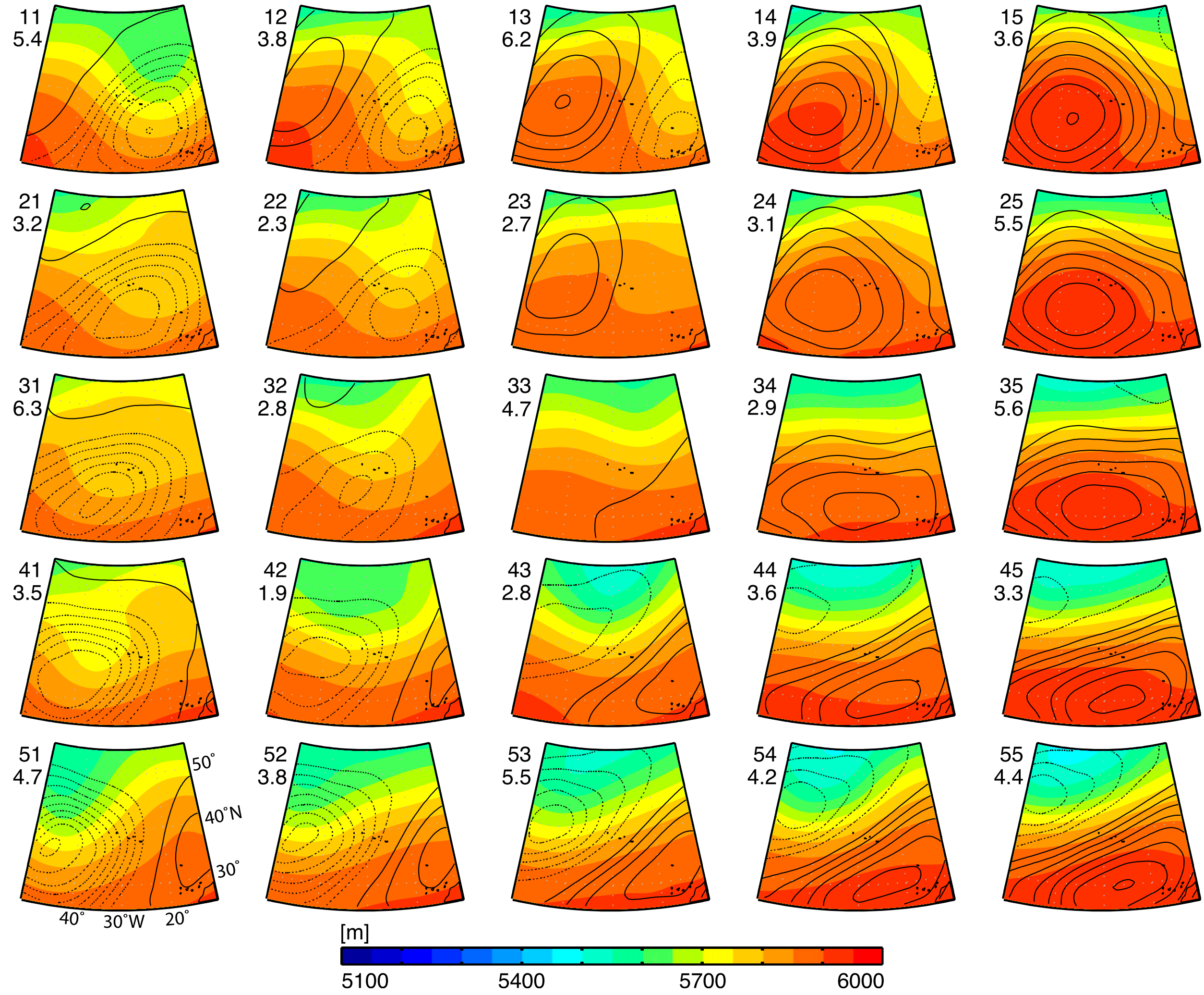

FIG. 3. Monthly-window SOM nodes of 500-hPa geopotential heights with overlaid contours of normalized 500-hPa geopotential height anomalies (using mean and standard deviation values calculated over a 31-day window centered on each day) for June. The contour interval for the height anomalies is 0.1 (nondimensional). The numbers associated with each node indicate node number in matrix notation and the relative frequency of occurrence of each node.

This exercise results in the annual cycle presented in Table 1 and shown in Fig. 4a, which indicates that all of the different synoptic configurations are present in each month. Particularly noteworthy is the result that June experiences synoptic intrusions (trough regimes) 20.5% of the time, a frequency greater than what might be expected given the dominant Bermuda high in the late spring and summertime months (the May and July percentages are also large, and for the same reason). This breakdown using month-by-month classifications accurately reflects the synoptic variability at any given time relative to what typically occurs in that month. We note, of course, that the trough classification in January is substantially different (much stronger) than the June trough classification.

Performing the SOM analysis using anomalies that are based on the mean and standard deviation from the entire dataset results in only a single classification (trough, pretrough, etc.) for the entire annual cycle. In this approach, the trough classification is characteristic of the strong troughs present during the winter, and the ridge classification represents conditions of the summertime Bermuda high. For this reason, summer is dominated by ridge and zonal patterns, whereas winter predominately features trough- and posttrough-type patterns (Table 2 and Fig. 4b). This annual perspective of the dataset (Fig. 4b) does not exhibit the trough classification during the summer months and therefore misses the synoptic intrusions identified in the monthly analysis shown in Fig. 4a. In a similar way, these anomalies indicate that the

TABLE 1. Percentages of synoptic patterns experienced during each month calculated using classifications that are based on anomalies calculated from monthly averaging windows.

	Pretrough	Trough	Posttrough	Ridge	Zonal	Unclassified
Jan	21.1	17.2	8.4	25.4	17.1	10.8
Feb	10.9	21.6	18.4	26.5	15.6	7.1
Mar	14.5	21.8	18.0	34.6	0.0	11.1
Apr	24.0	13.9	20.6	24.7	13.1	3.6
May	17.7	30.0	24.5	21.3	6.6	0.0
Jun	22.6	20.5	25.1	21.7	9.8	0.0
Jul	0.0	30.3	38.6	16.8	14	0.0
Aug	8.2	22.6	26.5	26.1	9.2	7.3
Sep	11.6	26.0	18.2	20.3	19.9	3.6
Oct	23.6	17.7	33.1	18.1	2.8	4.5
Nov	21.2	14.9	24.6	30.6	3.7	5.1
Dec	11.7	26.4	10.0	27.9	12.2	11.6

winter months are dominated almost exclusively by trough and posttrough weather patterns, without any ridge features. Figure 4a shows, on the other hand, that ridges are clearly present in the wintertime months.

The differences in these two approaches lie in how the classifications are defined. Using only a single SOM node space for the entire year means that winter months will tend to map to more troughlike nodes and summer months will map to more ridgelike nodes. Our analysis focuses on synoptic variability, and therefore anomalies that are based on monthly-window means (e.g., Fig. 4a) better characterize how any given synoptic state compares with climatological behavior in its given month.

Figure 5 shows that January or June in any given year may not be representative of the long-term average distribution of synoptic behavior. This result suggests that extreme caution should be used when interpreting the generality of conclusions reached from short-term field deployments and encourages long-term field-data collection efforts.

5. Dominant synoptic and cloud regimes—June

a. Synoptic properties

In the previous section, we classified nodes together according to synoptic category (trough, ridge, etc.) to calculate the frequency of each broad category. Compositing the synoptic and cloud structures themselves tends to overgeneralize the states for the purpose of interpretation of the synoptic and cloud structures. For this reason, we take the most-frequent nodes found on the middle edges of Fig. 3 as archetypes of the four synoptic patterns over the North Atlantic region in June. Figure 6 shows these dominant synoptic states in terms of the composited environmental variables. The pretrough pattern shows that the Azores lie in a tight gradient of 500-hPa heights, with the trough axis near the western portion of the domain. At 1000 hPa, a weak Bermuda high is present south and east of the Azores, and a low pressure center is present in the northwestern portion of the domain. This 1000-hPa trough is roughly collocated with the 500-hPa trough axis. The Bermuda high is least dominant in this synoptic state, reflected in its smallest spatial extent when compared with the other archetypes and the presence of the weak Icelandic low, which is present only in this pattern. The vertical-motion field is consistent with the 500-hPa geopotential-height field, specifically with upward vertical motion accompanying regions of positive differential vorticity advection downstream of the trough axis.

EIS exhibits a tongue of low values oriented from southwest to northeast, with smaller values equatorward and to the west. This tongue of low EIS values is present during June in all of the dominant states, and the fine details of the position and magnitude of this EIS tongue are consistent with the vertical-motion field. To be specific, areas of strong subsidence at 500 hPa are associated with greater stability and a westward displacement of the low-EIS tongue. In the pretrough state, the Azores experience low values of EIS and lie on the border between upward and downward vertical motion at 500 hPa, depending on the location of the trough axis at 500 hPa.

The trough pattern shows a weak positively tilted 500-hPa trough located over and to the southwest of the Azores. The 500-hPa trough is evidently not sufficiently strong to promote development of a surface low, but the pattern exhibits a weaker low-level Bermuda high than do the posttrough and ridge regimes. The weak trough does not exhibit the robust region of ascent downstream of the trough axis as in the pretrough pattern. Subsidence is widespread in this state, which encourages greater stability values across the northern and eastern portions of the domain (with the exception of the most northwestern portion of the domain, which is strongly influenced by extremely cold waters that enhance

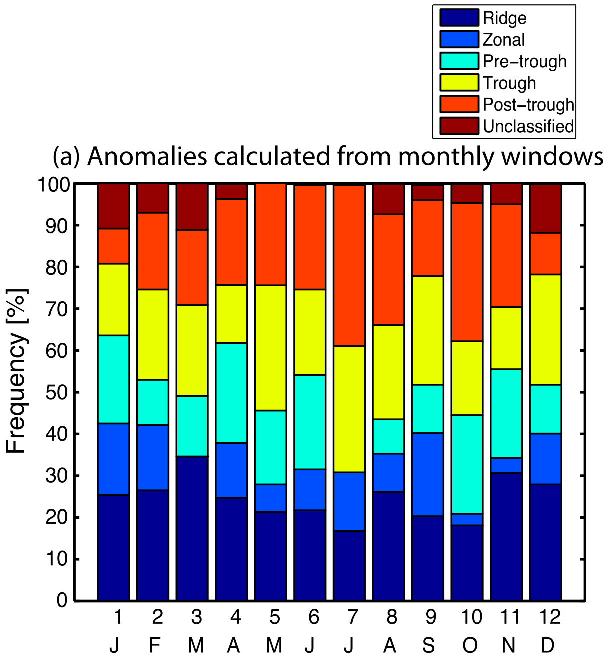

(b) Anomalies calculated from entire dataset

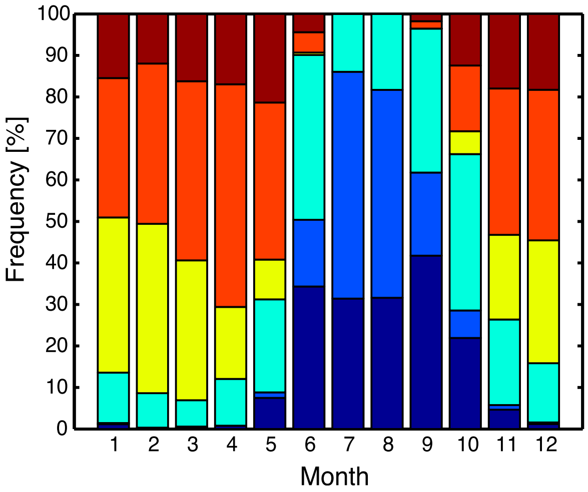

FIG. 4. Annual cycle of ridge, zonal, pretrough, trough, posttrough, and unclassified patterns as based on the anomalies calculated using (a) monthly averaging windows (calculated using the centered/running mean and standard deviation) or (b) a window that is the length of the entire dataset.

stability in the area). Over the Azores, both the trough and pretrough patterns exhibit similar EIS values.

The posttrough pattern shows the 500-hPa trough axis on the far eastern portion of the domain, with the Azores just east of a ridge axis. The Bermuda high is strong at this state and is collocated with the 500-hPa ridge axis. The tongue of low stability is restricted to the westernmost portion of the domain. The strongest subsidence is found in this synoptic state, with a maximum located downstream of the 500-hPa ridge axis. This strong subsidence promotes larger EIS values over the Azores relative to the pretrough and trough states, making this the most stable synoptic state experienced over the Azores region. A small region of low EIS values is associated with the trough axis on the easternmost region of the domain.

The ridge pattern exhibits the greatest 500-hPa heights, with the ridge axis centered over the Azores. The Bermuda high at 1000 hPa is similar in structure to that in the posttrough state, but the high pressure system is more centered over the Azores and does not extend as far north. Subsidence dominates much of the southern portion of the domain, with a maximum downstream of the ridge axis and the negative differential vorticity advection there. The EIS structure in the ridge regime is similar to the posttrough state, but the eastern portion of the domain is dominated by larger EIS values, likely because of more widespread subsidence leading to stronger stability. The Azores lie along a west–east gradient in stability, as they do in the posttrough state.

b. *Cloud properties*

Each of the four archetypal regimes in Fig. 6 exhibits a shield of cold clouds to the northwest, as well as warm, low stratocumulus clouds to the southeast. Figure 7 indicates that the ERA-I cloud fraction is systematically smaller than cloud-fraction estimates from MODIS, but patterns of cloud fraction and CTT are often in reasonable agreement. We chose to show the mean, but in principle any measure of central tendency could be used. Measures of variance or even the full probability distribution function (PDF) could be included as well.

In the pretrough state, the Azores lie within a strong gradient (northwest–southeast) in condensate and cloud fraction, with both quantities increasing toward the northwest. These cloud structures lie downstream of the trough axis in Fig. 6 and appear to be associated with areas of strong upward vertical motion. On average, these are mixed-phase clouds (CTT < 250 K). Condensate and cloud fraction decrease substantially toward the south and southeast, except for a small tongue of larger cloud fraction east and southeast of the Azores. This area of warm, low cloud (stratocumulus, most likely) is evident in both the MODIS data and the reanalysis. These low clouds lie in an area of subsidence and modestly stable values of EIS ($\sim$4–5 K). In this regime, the Azores lie near the strongest part of the gradient in cloud fraction and CTT and therefore may experience either low-altitude liquid stratocumulus or higher-altitude frontal clouds associated with synoptic systems that are influencing the region.

The trough pattern shows colder cloud tops displaced toward the south and southeast portions of the domain. In this regime, the Azores lie well inside the synoptic

TABLE 2. Percentages of synoptic patterns experienced during each month calculated using classifications that are based on anomalies calculated from the mean and standard deviation from the entire data record.

	Pretrough	Trough	Posttrough	Ridge	Zonal	Unclassified
Jan	12.1	37.4	33.6	1.1	0.3	15.5
Feb	8.3	40.8	38.6	0.3	0.0	12.0
Mar	6.4	33.7	43.2	0.4	0.2	16.2
Apr	11.3	17.4	53.6	0.8	0.0	17.0
May	22.4	9.6	37.9	7.5	1.3	21.3
Jun	39.7	0.6	4.9	34.3	16.1	4.4
Jul	13.9	0.0	0.0	31.4	54.6	0.0
Aug	18.3	0.0	0.0	31.6	50.1	0.0
Sep	34.7	0.0	1.8	41.8	20.0	1.8
Oct	37.7	5.5	15.8	21.9	6.6	12.4
Nov	20.6	20.4	35.3	4.6	1.1	18.0
Dec	14.3	29.6	36.3	1.2	0.4	18.3

cloud shield. The steepest gradient in ERA-I condensate, cloud fraction, and CTT is less evident in the MODIS cloud fields, which display a less coherent signal. In fact, the MODIS retrievals exhibit a substantial northward intrusion of warm cloud tops (low clouds) that in the reanalysis is present only over the easternmost portion of the domain. We find that ERA-I, relative to MODIS, has a smaller total cloud fraction and a lower cloud-top temperature in the trough regime. The cold cloud tops and smaller cloud fraction of ERA-I relative to MODIS suggest that ERA-I produces too little cloud overall but too much midlevel (~270 K) cloud in the trough regime.

In the posttrough state, total condensate is more extensive over the southeastern portion of the domain than in the pretrough and trough states. The area of strong subsidence in Fig. 6 and low CTTs for this pattern indicate that the majority of the clouds over and to the east, south, and southwest of the Azores are stratocumulus clouds. The spatial configurations of ERA-I and MODIS cloud fractions are very similar in this regime. These stratocumulus are found downstream of the 500-hPa ridge axis and over the eastern portion of the Bermuda high, in a region of stronger EIS values. The areas of maximum total condensate and maximum ERA-I and MODIS cloud fractions are collocated with areas of ascent in the northwestern portion of the domain and do not reach as far south as in the pretrough state. The warm cloud tops indicate that stratocumulus are the dominant cloud type over the Azores in the posttrough state.

Because of the strong gradient in vertical motion and strong subsidence downstream of the 500-hPa ridge axis (Fig. 6), the ridge pattern most clearly illustrates the different cloud regimes in the region. The area of ascent at 500 hPa in the far northwest is associated with condensate values as high as 200 g m^{-2}. The clouds associated with this total condensate are cold (~260 K for both MODIS and reanalysis) and spatially extensive, with their boundary in the vicinity of the Azores. Beginning north of the Azores, the cloud field makes a transition to warmer (i.e., lower) cloud toward the south. This stratocumulus deck is encouraged by the subsidence maximum in this state and lies in an area of stronger stability. Stratocumulus are most extensive in this ridge pattern, which may be attributed to having such high values of subsidence downstream of the ridge axis. In this regime, cloud conditions at the Azores are influenced by the southeastern stratocumulus deck and the relatively clear slot to the southwest, which may modulate the Azores cloud field. The overlapping of the regimes suggests an environment that is conducive to substantial variability in cloud properties at the Azores.

The length of each shade of gray in the vertical bars in Fig. 7 is proportional to the frequency of occurrence for three different cloud-fraction ranges loosely corresponding to mostly clear (<0.1), cloudy (0.1–0.9), and nearly overcast (>0.9). In effect, these bars are a highly distilled form of the cloud-fraction PDF. These show that cloud cover is predominant for all regimes but for the most part is less than overcast and rarely clear.

In summary, these June cloud regimes suggest substantial variability in cloud properties over the Azores. The Azores are located in a prime location to experience both stratocumulus clouds and clouds associated with synoptic low pressure systems. The position of the 500-hPa wave and its associated vertical motion field influence the cloud properties over the region.

6. Dominant synoptic and cloud regimes—January

a. Synoptic properties

The four synoptic configurations in Fig. 8 differ substantially from the June patterns. In the pretrough regime, the Azores lie in a region of weak ascent and

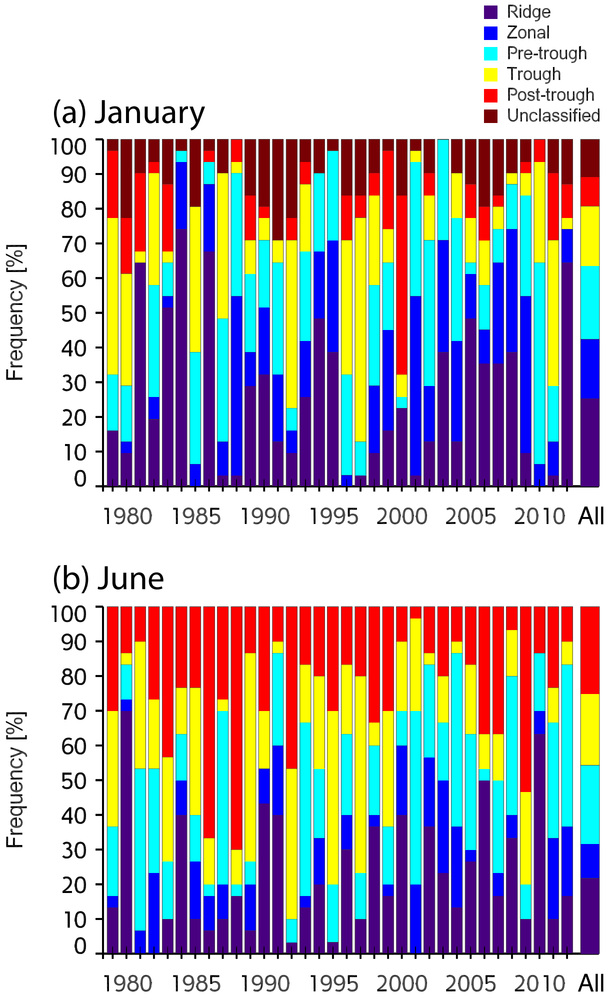

FIG. 5. Year-by-year time series of ridge, zonal, pretrough, trough, posttrough, and unclassified patterns as based on the monthly-window anomalies for (a) January and (b) June. The rightmost bars shows the mean breakdown for all years and are equivalent to the January and June bars in Fig. 4a.

relatively low stability. The pretrough pattern for January has strong north–south gradients in 500-hPa geopotential heights, indicative of a jetlike structure with a maximum in the vicinity of the Azores. The trough axis is difficult to discern but lies west of the Azores. The 1000-hPa structure resembles a confluent trough and also exhibits a strong north–south gradient. Given the jet structure at 500 hPa, the southwestern and northeastern regions of the domain constitute the right-entrance and left-exit regions—an interpretation that is consistent with regions of ascent in the 500-hPa vertical velocity field. In broad terms, the magnitude of vertical velocity in January is much greater than in June. Regions of ascent are associated with smaller EIS values; stronger subsidence coincides with greater stability. The far northwestern region of the domain is the most stable, and this feature is present in all of the synoptic patterns (and in June as well) because of the cold surface temperatures in this area. The baseline ‘‘tongue’’ of low EIS values seen consistently in June (Fig. 6) is not present in January, when EIS varies much more across the different synoptic regimes.

The trough regime has an easily distinguishable trough axis lying just west of the Azores. At 1000 hPa, the Icelandic low is so dominant that the Bermuda high is not present. The Icelandic (surface) low is centered northwest of the islands, with its trough axis just downstream of the upper-level trough axis. Most of the center portion of the domain, including the Azores region, is dominated by strong ascent, although subsidence is present in the western and north-northeastern regions of the domain. This strongest ascent in the center of the domain corresponds to a bull’s-eye of the lowest EIS values.

The posttrough regime is characterized by a positively tilted ridge–trough pair. The 500-hPa ridge axis is oriented from the southwest to the northeast over the western part of the domain, and the trough axis is located across the southeastern corner of the domain. This positively tilted ridge encourages the presence of an elongated Bermuda high, with its maximum directly north of the Azores. Strong subsidence is present over and downstream of the ridge axis (both 500 and 1000 hPa), across a region characterized by high values of 1000-hPa geopotential height. Enhanced stability accompanies much of this large region of subsidence, with the Azores lying near a strong gradient in EIS. Weak stability is found downstream of the trough axis in a region of ascent next to the African coastline.

A positively tilted 500-hPa ridge lying over the Azores characterizes the ridge regime. Large values of 1000-hPa geopotential height show the presence of a strong Bermuda high, centered just east of the Azores, that dominates much of the analysis domain. A dipole of vertical velocity straddles the ridge, with subsidence present over the eastern half of the high and ascent west of the 500-hPa ridge axis. The influence of the vertical velocity couplet is evident in the intrusion of low EIS to the west of the Azores and a region of high stability to the east. Large values of EIS are found in the northern and eastern portions of the domain, the latter region being where stratocumulus decks tend to persist in the summertime months. In the January ridge regime, however, subsidence and stability are even stronger and more spatially widespread than in June.

January shows much more variability across the different synoptic regimes than does June. Regions of substantial large-scale ascent associated with midlatitude synoptic systems reach lower latitudes in winter, allowing these latitudes to experience sustained periods

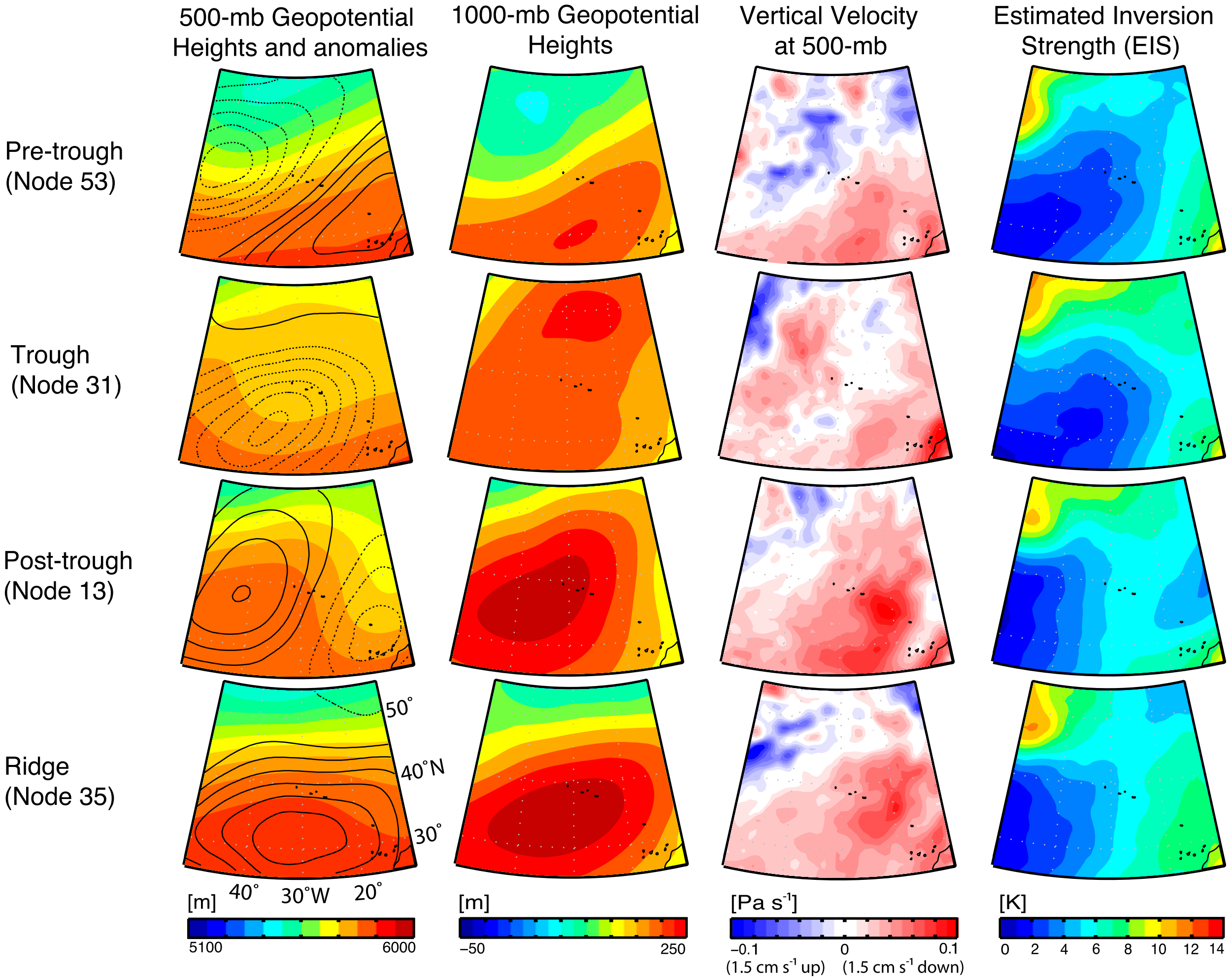

FIG. 6. Synoptic properties for the four archetypal synoptic regimes in June (calculated from the monthly averaging windows using the centered/running mean and standard deviation), including 500-hPa geopotential heights and anomalies, 1000-hPa geopotential height, 500-hPa vertical velocity, and EIS.

of ascent. January exhibits both stronger ascent and descent than June, and the Azores lie along the transition between ascent and descent (pretrough and ridge regimes). The Icelandic low exerts a strong influence during wintertime months and seems to be the ultimate source of much of the meteorological variability across the patterns, as the low develops and modulates the strength and persistence of the Bermuda high.

b. Cloud properties

Mean January cloud properties associated with each characteristic synoptic regime (Fig. 9) show that the synoptic and cloud structures exhibit more variation across the pattern than the characteristic patterns for June (cf. Fig. 7). In the pretrough state, large values of cloud fraction are present over the majority of the domain in both the reanalysis and MODIS, except for the most southeast and southwest regions. The total condensate field shows a strong gradient across the Azores and a local maximum in total condensate in the northeastern portion of the domain associated with the strong ascent from the left-exit region of the jetlike structure in this synoptic pattern (Fig. 8). ERA-I and MODIS show similar structures across the domain, but, as previously seen, MODIS cloud fractions are greater than those from the reanalysis. Large values of cloud fraction prevail across most of the domain, but differences in cloud-top temperature between MODIS and the reanalysis suggest differences in cloud type and behavior in the two datasets. The coldest clouds in the reanalysis CTT lie in the area of ascent and are located in the northern portions of the domain, extending southward to the Azores. In the middle of the most southern portion of the domain, however, clouds are present in both the total

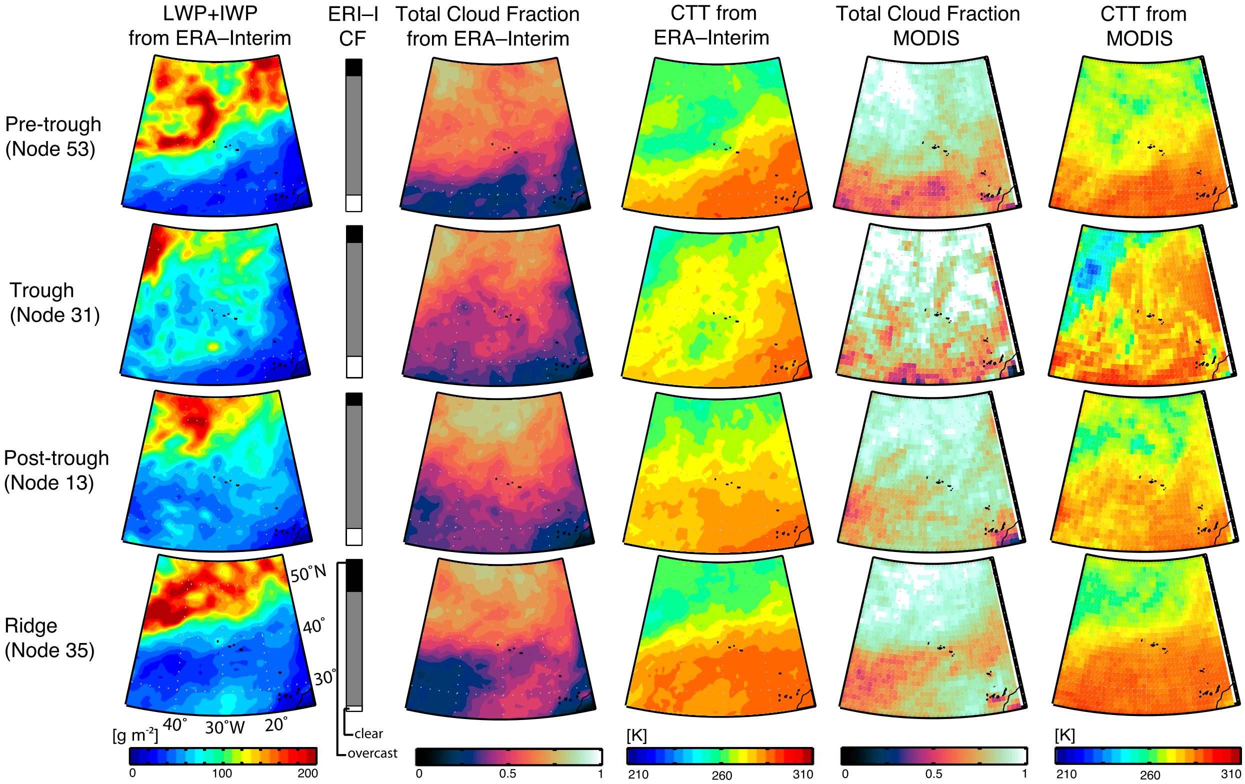

FIG. 7. Cloud properties for the four archetypal synoptic regimes in June. For each regime, fields plotted are total ERA-I condensate, total cloud fraction, and CTT, as well as total cloud fraction and CTT from MODIS. The length of each shade of gray in the vertical bars is proportional to the frequency of occurrence for cloud fractions of 0.0–0.1 (white, labeled "clear" in the figure), 0.1–0.9 (gray), and 0.9–1.0 (dark gray, labeled "overcast") at the ERA-I grid point nearest to the Azores.

condensate and total cloud fraction for the reanalysis and MODIS. These clouds must be stratocumulus because of their warm CTT values (around 280 K), higher cloud fraction (close to 1.0 from MODIS), and lower total condensate values (around 60 g m^{-2}).

The spatial structure of the reanalysis condensate in the trough regime is oriented in a north–south configuration, with a maximum located just east of the trough axis in Fig. 8. These large values of condensate are also associated with the location of strong ascent and weak stability. The CTT field from both the reanalysis and MODIS identifies these as cold clouds. This band of cold cloud tops, however, is narrower in MODIS than in the reanalysis, and the MODIS cloud band is more distinguishable in the CTT field than in the cloud fraction. The cloud-property structures (particularly total condensate and MODIS CTT) are strikingly similar to the vertical velocity field.

In the posttrough state, clouds in the northwestern part of the domain are strongly tied to the region of ascent upstream of the ridge axis (Fig. 8). Across the southeast, both the reanalysis and MODIS show a pocket of cold clouds in a region of ascent downstream of the trough axis. The area between the northwestern cloud regime and the southeastern cold pocket is composed of warmer clouds in a region of subsidence, suggesting stratocumulus. These clouds lie in a strong gradient from weaker to stronger EIS, an unusual feature in comparison with other regimes in which stratocumulus is associated with broad regions of strong stability. These clouds appear to be largely consistent with the post-cold-frontal stratocumulus seen in Mechem et al. (2010).

As in June, the January ridge state exhibits two well-defined cloud regimes, as evident in the reanalysis total condensate and reanalysis and MODIS cloud-top temperature. These cloud regimes represent mixed-phase clouds toward the north and clouds in the eastern ocean basin. The distinct couplet of these cloud types is associated with the vertical velocity and stability couplets from Fig. 8. The northwestern region is dominated by ascent and exhibits widespread cold clouds and total condensate values of 200 g m^{-2}. Cold cloud-top temperatures of ~260 K extend to the Azores. In the subsidence region associated with higher stability downstream of the ridge axis in Fig. 8, warmer cloud-top temperatures and lower

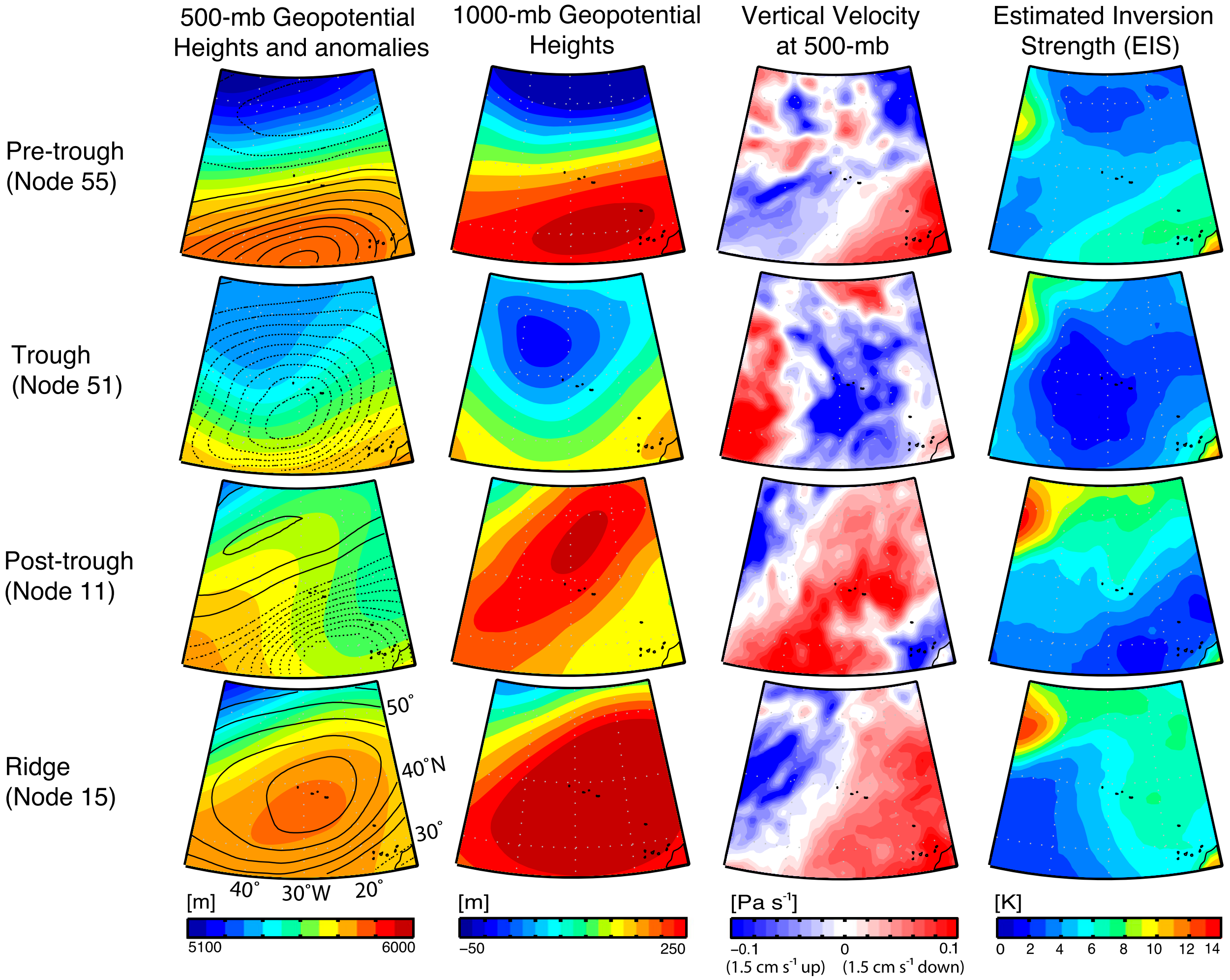

FIG. 8. As in Fig. 6, but for January. The 5 × 5 node map for January from which these specific nodes are drawn (corresponding to Fig. 3 for the June nodes) is shown in supplemental Fig. S1.

total condensate values persist, suggesting stratocumulus. The location and spatial coverage of these stratocumulus are similar to the stratocumulus location and coverage in the June ridge regime.

One common theme of these analyses is that the Azores in January, as in June, lie in a region of overlapping cloud types. The January synoptic regimes are associated with substantial cloudiness, although details of cloud structure differ and regions of clear (cloud fraction < 0.1; see the vertical bars in Fig. 9) are more common than during June. Relative to June, January exhibits far greater synoptic and cloud variability in both magnitude and spatial distribution. In January, the Icelandic low is predominantly responsible for the modulation of the Bermuda high, and stratocumulus are associated with locations of 500-hPa subsidence. The cloud distribution as shown in the vertical bars in Fig. 9 indicates greater differences in near-clear and near-overcast cloud cover over the Azores relative to June conditions.

7. Discussion and conclusions

De Szoeke et al. (2016) showed larger or similar variance in marine low-cloud cover associated with multiday synoptic variability as compared with seasonal variability in subtropical marine stratocumulus regions. Characterizing synoptic context is vital in developing insight into how MBL cloud properties respond to synoptic-scale forcing mechanisms on multiday time scales. Constraining synoptic conditions is also a prerequisite to untangling internal cloud-system aerosol–cloud–precipitation interactions. We chose to base our classification on synoptic states and then composite cloud properties on those synoptic states, the justification being that cloud properties are to first order an

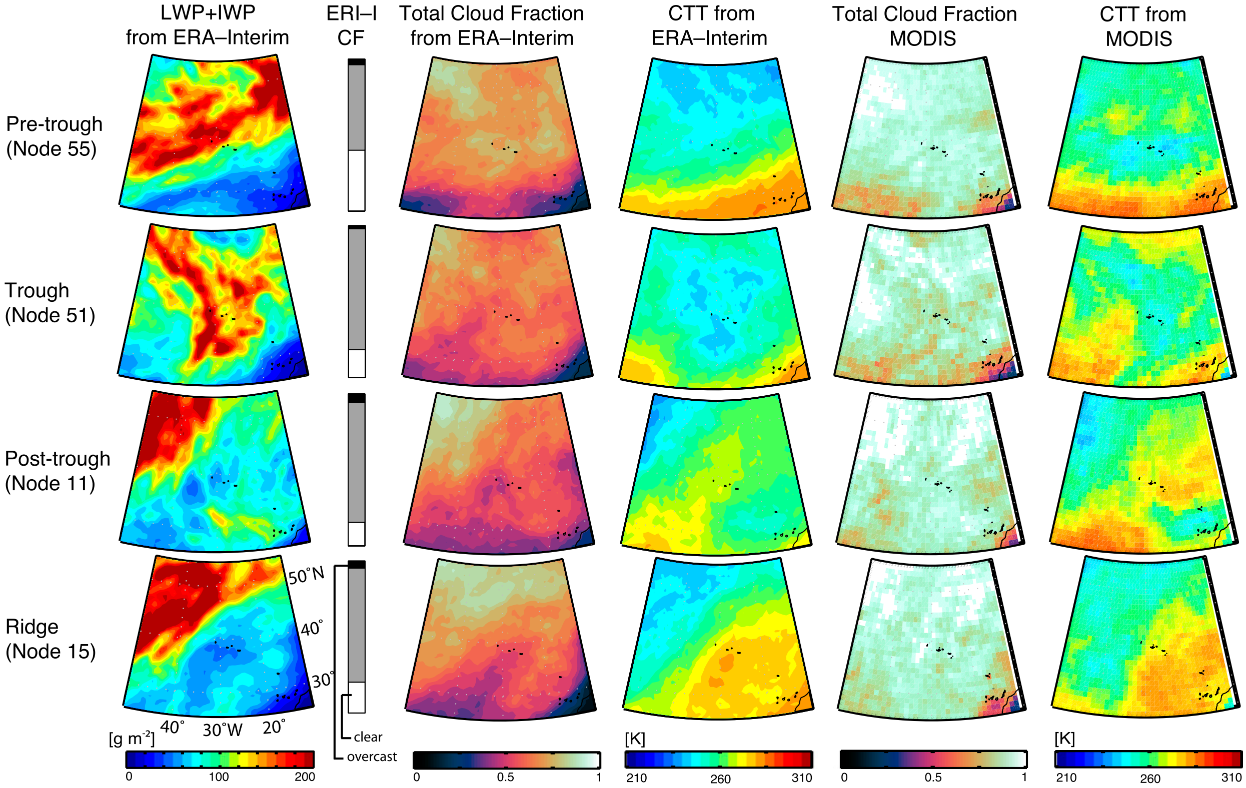

FIG. 9. As in Fig. 7, but for January.

outcome of the synoptic-scale environment and forcing. The alternate approach, a clustering on the basis of cloud properties (e.g., Rémillard and Tselioudis 2015), raises the possibility that similar clouds can occur under different synoptic states, making a clear attribution to specific forcing mechanisms a challenge. An example of clouds with similar physical characteristics originating under different conditions is low marine clouds in regions with strong subsidence versus those in cold-air outbreaks.

We employ the technique of self-organizing maps to develop a climatological description of synoptic and cloud patterns centered on the Azores islands in the eastern North Atlantic. The SOM approach, which in this paper is based on classifying normalized 500-hPa geopotential height anomalies, is successful in identifying dominant synoptic states. Compositing meteorological and cloud properties by synoptic pattern provides insights into how clouds and their environment jointly vary by synoptic state. The SOM approach identifies well-established patterns consistent with a long-standing understanding of the structure of midlatitude baroclinic synoptic waves, and it does so in an objective manner that can be applied to large datasets. For example, the SOM method could be employed to evaluate the cloud behavior in climate models as a function of synoptic regime. Unlike linear techniques such as principal component analysis/EOF approaches, the SOM method preserves the continuity across the different synoptic states.

Our discussion focuses on June and January because of their significance in the annual cloud cycle. The Azores island chain (~39°N) consistently lies in an area of substantial variability in both synoptic configuration and environmental and cloud properties in comparison with the persistent MBL stratocumulus regimes in the northeastern Pacific Ocean, southeastern Pacific, and southeastern Atlantic [25°N, 18°S, and 15°S, respectively; Fig. 4 in Wood (2012)]. The Azores has long been considered a "transition" region in terms of cloud-regime transitions accompanying SST gradients (Albrecht et al. 1995). It is *also* a transition region between the influences of the semipermanent subtropical highs and midlatitude synoptic waves. The synoptic-scale variability has been largely underappreciated even though it strongly modulates large-scale vertical motions and cloudiness. There are frequently occurring high and middle clouds throughout the year [e.g., the daylight high-cloud amount over the Azores of ~0.3 in Fig. 1a of de Szoeke et al. (2016)] so the radiative effects of low clouds without high clouds above them occur for only a fraction of the domain and a portion of the time.

Variability on synoptic time scales is most evident when the SOM classification is performed on anomalies calculated using monthly-window means and standard deviations, which act as a high-pass filter that removes multimonth (seasonal) and longer variability. Ridges, troughs, and transitional patterns are present for both January and July, but these patterns must be understood in the context of both the monthly and annual climatological behavior to be interpreted correctly. A trough in January, for example, is more intense (lower heights and stronger height gradient) than a trough in June. The Azores exhibits a combination of the northern, cold, thick regime as well as the low cloud tops of stratocumulus. The highly variable nature of the clouds in the Azores can be partially attributed to overlapping cloud regimes.

June is dominated by the Bermuda high, and patterns with a weaker Bermuda high permit synoptic intrusions into lower latitudes. There are an advance and retreat of high-level clouds coming from the north that appear to covary in association with vertical velocity. The edge of the stratocumulus deck exhibits a sloshing back and forth (west to east) along a roughly west-southwest–east-northeast diagonal over the Azores (Fig. 7; the mean column-total condensate for each node, which is illustrated in Fig. S13 of the online supplemental material, provides a more complete picture of this movement of the stratocumulus edge across all the node space). We note that this sloshing effect is a manifestation of substantial spatial and/or temporal variability. When the upper-level ridge axis is centered over the Azores, associated subsidence conditions east and southeast of the Azores create ideal conditions for stratocumulus persistence. The baseline tongue structure of EIS is modulated by sustained vertical velocity fields, with subsidence associated with increased stability. Stratocumulus are dominant downstream of this ridge axis, in regions of high stability. The summer months have the highest amounts of low-level clouds at the Azores. From anomalies calculated relative to the entire dataset (Table 2), during June the relative frequencies of different synoptic patterns in order of frequency of occurrence are pretrough (40%), ridge (34%), zonal flow (16%), posttrough (5%), unclassified (4%), and trough (<1%). When the seasonal variability is removed by running the SOM analysis on the running monthly anomalies, the frequency of occurrence of the different synoptic patterns in June is more evenly distributed among the nodes, with 25% posttrough, 23% pretrough, 22% ridge, 20% trough, and 10% zonal flow (Table 1).

January exhibits greater spatial variability in synoptic and cloud properties and larger differences in magnitude among synoptic patterns than is observed in June. Instead of the Bermuda high dominating synoptic properties, the Icelandic low modulates most aspects of the synoptic regimes over the region. Although the low pressure centers associated with winter extratropical cyclones in the northeastern Atlantic are usually well north of the Azores, the southern portions of cold fronts can drape over the islands. Again, there is a sloshing back and forth both in the advance and retreat of high-level clouds coming from the north that penetrate farther south than in June (cf. Figs. 7 and 9). Low clouds occur to the southeast of the Azores with the cloud deck western edge forming a southwest–northeast diagonal that bisects the island chain during monthly anomaly ridge conditions (Fig. 9). From anomalies calculated relative to the entire dataset (Table 2), during January the relative frequencies of different synoptic patterns in order of frequency of occurrence are trough (37%), posttrough (34%), unclassified (15%), pretrough (12%), ridge (1%), and zonal flow (<1%). When the seasonal variability is removed by running SOM on the running monthly anomalies, the frequency of occurrence of the different synoptic patterns in January is 25% ridge, 21% pretrough, 17% trough, 17% zonal flow, 10% unclassified, and 8% posttrough (Table 1). In winter, stratocumulus near the Azores primarily occur as post-cold-frontal stratocumulus with the posttrough regime (Mechem et al. 2010).

The SOM approach outlined here is a general, robust, and broadly applicable method of characterizing synoptic regimes for any given region. Depending on the application, anomalies calculated relative to multiyear annual means, relative to running monthly means, or both may be appropriate. These classifications can place case studies into the context of their synoptic environment as well as that of the multidecade sample. For longer-term datasets, this method can identify dates or periods with certain synoptic characteristics for focused study and could be used to explore the change in synoptic patterns over time. Last, our results show that the relative occurrence of synoptic patterns in any single year or any given month at the Azores is unlikely to be representative of the climatological behavior, suggesting caution when inferring long-term conditions from short-term field campaigns. Furthermore, the lack of a representative sample of synoptic regimes over a short field campaign could well introduce substantial and misleading uncertainties in cloud properties as well.

Acknowledgments. The authors greatly appreciate advice and feedback from Adriana Bailey, Aaron Kennedy, and Shu Chen. Many thanks are given to Maike Ahlgrimm for her tireless patience in answering our many questions about ERA-Interim details. Thanks are also given to Lucas McMichael for comments on the manuscript. We appreciate the thoughtful reviews from

Tim Myers, Aaron Kennedy, and an additional anonymous reviewer, who helped to clarify various aspects of the manuscript. This work was funded by U.S. Department of Energy Atmospheric Systems Research Grants DE-SC0006736 (to author Mechem), DE-SC0016522 (to Mechem), DE-SC0006701 (to author Yuter), and DE-SC0006994 (to author de Szoeke). Author Mechem also acknowledges support through the Office of Naval Research Award N00014-11-1-0518.

REFERENCES

Abercromby, R., 1883: On certain types of British weather. *Quart. J. Roy. Meteor. Soc.*, **9**, 1–25, https://doi.org/10.1002/qj.4970094502.

Albrecht, B. A., C. S. Bretherton, D. Johnson, W. H. Schubert, and A. S. Frisch, 1995: The Atlantic Stratocumulus Experiment—ASTEX. *Bull. Amer. Meteor. Soc.*, **76**, 889–904, https://doi.org/10.1175/1520-0477(1995)076<0889:TASTE>2.0.CO;2.

Ambroise, C., F. Badran, and S. Thiria, 2000: Hierarchical clustering of self-organizing maps for cloud classification. *Neurocomputing*, **30**, 47–52, https://doi.org/10.1016/S0925-2312(99)00141-1.

Bailey, A., T. N. Chase, J. J. Cassano, and D. Noone, 2011: Changing temperature inversion characteristic in the U.S. Southwest and relationships to large-scale atmospheric circulation. *J. Appl. Meteor. Climatol.*, **50**, 1307–1323, https://doi.org/10.1175/2011JAMC2584.1.

Balling, R. C., 1984: Classification in climatology. *Spatial Statistics and Models*, G. L. Gaile and C. J. Willmott, Eds., D. Reidel, 81–108.

Betts, A. K., and A. Beljaars, 2017: Analysis of near-surface biases in ERA-Interim over the Canadian prairies. *J. Adv. Model. Earth Syst.*, **9**, 2158–2173, https://doi.org/10.1002/2017MS001025.

Burleyson, C. D., S. P. de Szoeke, S. E. Yuter, M. Wilbanks, and W. A. Brewer, 2013: Ship-based observations of the diurnal cycle of southeast Pacific marine stratocumulus clouds and precipitation. *J. Atmos. Sci.*, **70**, 3876–3894, https://doi.org/10.1175/JAS-D-13-01.1.

Caldwell, P., C. S. Bretherton, and R. Wood, 2005: Mixed-layer budget analysis of the diurnal cycle of entrainment in southeast Pacific stratocumulus. *J. Atmos. Sci.*, **62**, 3775–3791, https://doi.org/10.1175/JAS3561.1.

Cassano, E. N., A. H. Lynch, J. J. Cassano, and M. R. Koslow, 2006: Classification of synoptic patterns in the western Arctic associated with extreme events at Barrow, Alaska, USA. *Climate Res.*, **30**, 83–97, https://doi.org/10.3354/cr030083.

Cavazos, T., 2000: Using self-organizing maps to investigate extreme climate events: An application to wintertime precipitation in the Balkans. *J. Climate*, **13**, 1718–1732, https://doi.org/10.1175/1520-0442(2000)013<1718:USOMTI>2.0.CO;2.

Coopman, Q., T. J. Garrett, J. Riedi, S. Eckhardt, and A. Stohl, 2016: Effects of long-range aerosol transport on the microphysical properties of low-level liquid clouds in the arctic. *Atmos. Chem. Phys.*, **16**, 4661–4674, https://doi.org/10.5194/acp-16-4661-2016.

Dee, D. P., and Coauthors, 2011: The ERA-Interim reanalysis: Configuration and performance of the data assimilation system. *Quart. J. Roy. Meteor. Soc.*, **137**, 553–597, https://doi.org/10.1002/qj.828.

de Szoeke, S. P., K. L. Verlinden, S. E. Yuter, and D. B. Mechem, 2016: The time scales of variability of marine low clouds. *J. Climate*, **29**, 6463–6481, https://doi.org/10.1175/JCLI-D-15-0460.1.

Gong, D., and S. Wang, 1999: Definition of Antarctic Oscillation Index. *Geophys. Res. Lett.*, **26**, 459–462, https://doi.org/10.1029/1999GL900003.

Hasanean, H., 2004: Variability of the North Atlantic subtropical high and associations with tropical sea-surface temperature. *Int. J. Climatol.*, **24**, 945–957, https://doi.org/10.1002/joc.1042.

Hewitson, B. D., and R. G. Crane, 1992: Regional-scale climate prediction from the GISS GCM. *Global Planet. Change*, **5**, 249–267, https://doi.org/10.1016/0921-8181(92)90014-2.

——, and ——, 2002: Self-organizing maps: Applications to synoptic climatology. *Climate Res.*, **22**, 13–26, https://doi.org/10.3354/cr022013.

Jakobson, E., T. Vihma, T. Palo, L. Jakobson, H. Keernik, and J. Jaagus, 2012: Validation of atmospheric reanalyses over the central Arctic Ocean. *Geophys. Res. Lett.*, **39**, L10802, https://doi.org/10.1029/2012GL051591.

Kennedy, A. D., X. Dong, B. Xi, S. Xie, Y. Zhang, and J. Chen, 2011: A comparison of MERRA and NARR reanalyses with the DOE ARM SGP data. *J. Climate*, **24**, 4541–4557, https://doi.org/10.1175/2011JCLI3978.1.

——, ——, and ——, 2016: Cloud fraction at the ARM SGP site: Reducing uncertainty with self-organizing maps. *Theor. Appl. Climatol.*, **124**, 43–54, https://doi.org/10.1007/s00704-015-1384-3.

Klein, S. A., 1997: Synoptic variability of low-cloud properties and meteorological parameters in the subtropical trade wind boundary layer. *J. Climate*, **10**, 2018–2039, https://doi.org/10.1175/1520-0442(1997)010<2018:SVOLCP>2.0.CO;2.

——, D. L. Hartmann, and J. R. Norris, 1995: On the relationships among low-cloud structure, sea surface temperature, and atmospheric circulation in the summertime northeast Pacific. *J. Climate*, **8**, 1140–1155, https://doi.org/10.1175/1520-0442(1995)008<1140:OTRALC>2.0.CO;2.

Kohonen, T., 2001: *Self-Organizing Maps*. 3rd ed. Springer, 501 pp.

——, J. Hynninen, J. Kangas, and J. Laaksonen, 1996: SOM_PAK: The self-organizing map program package. Helsinki University of Technology Laboratory of Computer and Information Science Rep. A31, http://www.cis.hut.fi/research/som-research/nnrc-programs.shtml.

Köppen, W., 1874: Über die Abhängigkeit des klimatischen Charakters der Winde von ihrem Ursprunge (On the dependence of the climatological characteristics of the winds on their trajectory). *Reportorium für Meteor.*, **4** (4), 15 pp.

Lamb, H. H., 1950: Types and spells of weather around the year in the British Isles: Annual trends, seasonal structure of the year, singularities. *Quart. J. Roy. Meteor. Soc.*, **76**, 393–429, https://doi.org/10.1002/qj.49707633005.

Lau, N.-C., and M. W. Crane, 1995: A satellite view of the synoptic-scale organization of cloud properties in midlatitude and tropical circulation systems. *Mon. Wea. Rev.*, **123**, 1984–2006, https://doi.org/10.1175/1520-0493(1995)123<1984:ASVOTS>2.0.CO;2.

——, and ——, 1997: Comparing satellite and surface observations of cloud patterns in synoptic-scale circulation systems. *Mon. Wea. Rev.*, **125**, 3172–3189, https://doi.org/10.1175/1520-0493(1997)125<3172:CSASOO>2.0.CO;2.

Li, W., L. Li, R. Fu, Y. Deng, and H. Wang, 2011: Changes to the North Atlantic subtropical high and its role in the intensification of summer rainfall variability in the southeastern United States. *J. Climate*, **24**, 1499–1506, https://doi.org/10.1175/2010JCLI3829.1.

Mechem, D. B., Y. L. Kogan, and D. M. Schultz, 2010: Large eddy observations of post-cold-frontal continental stratus. *J. Atmos. Sci.*, **67**, 3368–3383, https://doi.org/10.1175/2010JAS3389.1.

Myers, T. A., and J. R. Norris, 2013: Observational evidence that enhanced subsidence reduces subtropical marine boundary layer cloudiness. *J. Climate*, **26**, 7507–7524, https://doi.org/10.1175/JCLI-D-12-00736.1.

Norris, J. R., 1998: Low cloud type over the ocean from surface observations. Part I: Relationship to surface meteorology and the vertical distribution of temperature and moisture. *J. Climate*, **11**, 369–382, https://doi.org/10.1175/1520-0442(1998)011<0369:LCTOTO>2.0.CO;2.

——, and S. A. Klein, 2000: Low cloud type over the ocean from surface observations. Part III: Relationship to vertical motion and the regional synoptic environment. *J. Climate*, **13**, 245–256, https://doi.org/10.1175/1520-0442(2000)013<0245:LCTOTO>2.0.CO;2.

Oreopoulos, L., and M. Khairoutdinov, 2003: Overlap properties of clouds generated by a cloud-resolving model. *J. Geol. Res.*, **108**, 4479–4488, https://doi.org/10.1029/2002JD003329.

Platnick, S., M. D. King, S. A. Ackerman, W. P. Menzel, B. A. Baum, J. C. Riedi, and R. A. Frey, 2003: The MODIS cloud products: Algorithms and examples from *Terra*. *IEEE Trans. Geosci. Remote Sens.*, **41**, 459–473, https://doi.org/10.1109/TGRS.2002.808301.

Rémillard, J., and G. Tselioudis, 2015: Cloud regime variability over the Azores and its application to climate model evaluation. *J. Climate*, **28**, 9707–9720, https://doi.org/10.1175/JCLI-D-15-0066.1.

——, P. Kollias, E. Luke, and R. Wood, 2012: Marine boundary layer cloud observations in the Azores. *J. Climate*, **25**, 7381–7398, https://doi.org/10.1175/JCLI-D-11-00610.1.

Reusch, D. B., R. B. Alley, and B. C. Hewitson, 2007: North Atlantic climate variability from a self-organizing map perspective. *J. Geophys. Res.*, **112**, D02104, https://doi.org/10.1029/2006JD007460.

Schuenemann, K. C., J. J. Cassano, and J. Finnis, 2009: Synoptic forcing of precipitation over Greenland: Climatology for 1961–99. *J. Hydrometeor.*, **10**, 60–78, https://doi.org/10.1175/2008JHM1014.1.

Seidel, D. J., Y. Zhang, A. Beljaars, J.-C. Golaz, A. R. Jacobson, and B. Medeiros, 2012: Climatology of the planetary boundary layer over the continental United States and Europe. *J. Geophys. Res.*, **117**, D17106, https://doi.org/10.1029/2012JD018143.

Stevens, B., G. Vali, K. Comstock, M. C. Van Zanten, P. H. Austin, C. S. Bretherton, and D. H. Lenschow, 2005: Pockets of open cells (POCs) and drizzle in marine stratocumulus. *Bull. Amer. Meteor. Soc.*, **86**, 51–57, https://doi.org/10.1175/BAMS-86-1-51.

Tibshirani, G., G. Walther, and T. Hastie, 2001: Estimating the number of clusters in a data set via the gap statistic. *J. Roy. Stat. Soc.*, **63**, 411–423, https://doi.org/10.1111/1467-9868.00293.

Vesanto, J., and E. Alhoniemi, 2000: Clustering of the self-organizing map. *IEEE Trans. Neural Networks*, **11**, 586–600, https//doi.org/10.1109/72.846731.

Wood, R., 2012: Stratocumulus clouds. *Mon. Wea. Rev.*, **140**, 2373–2423, https://doi.org/10.1175/MWR-D-11-00121.1.

——, and C. S. Bretherton, 2006: On the relationship between stratiform low cloud cover and lower-tropospheric stability. *J. Climate*, **19**, 6425–6432, https://doi.org/10.1175/JCLI3988.1.

——, and D. L. Hartmann, 2006: Spatial variability of liquid water path in marine low cloud: The importance of mesoscale cellular convection. *J. Climate*, **19**, 1748–1764, https://doi.org/10.1175/JCLI3702.1.

——, and Coauthors, 2015: Clouds, Aerosol, and Precipitation in the Marine Boundary Layer: An ARM Mobile Facility deployment. *Bull. Amer. Meteor. Soc.*, **96**, 419–440, https://doi.org/10.1175/BAMS-D-13-00180.1.

DOI of main article: 10.1175/JAMC-D-17-0211.1; *Journal of Applied Meteorology and Climatology*

Joint Synoptic and Cloud Variability over the Northeast Atlantic near the Azores

David B. Mechem and Carly S. Wittman

Department of Geography and Atmospheric Science, University of Kansas, Lawrence, Kansas

Matthew A. Miller and Sandra E. Yuter

Department of Marine, Earth, and Atmospheric Sciences, North Carolina State University, Raleigh, North Carolina

Simon P. de Szoeke

College of Oceanic and Atmospheric Sciences, Oregon State University, Corvallis, Oregon

Supplemental Material

Supplemental figures

The supplemental figures S1–S12 represent the SOM nodes of 500-mb geopotential height with overlaid contours of normalized 500-mb geopotential height anomalies for the given month. These nodes are calculated from the anomalies obtained from mean and standard deviation values taken over 31-day centered windows. The SOM node map in Figure S6 is equivalent to that in Fig. 2 in the manuscript but is included for completeness. The supplemental figures also include the classification of each node into different synoptic categories, as described in the text.

Supplemental figure S13 represents the mean column-total condensate from Era–Interim for all 25 nodes for June in order to show the “sloshing” back and forth of the edge of marine low clouds associated with different synoptic states.

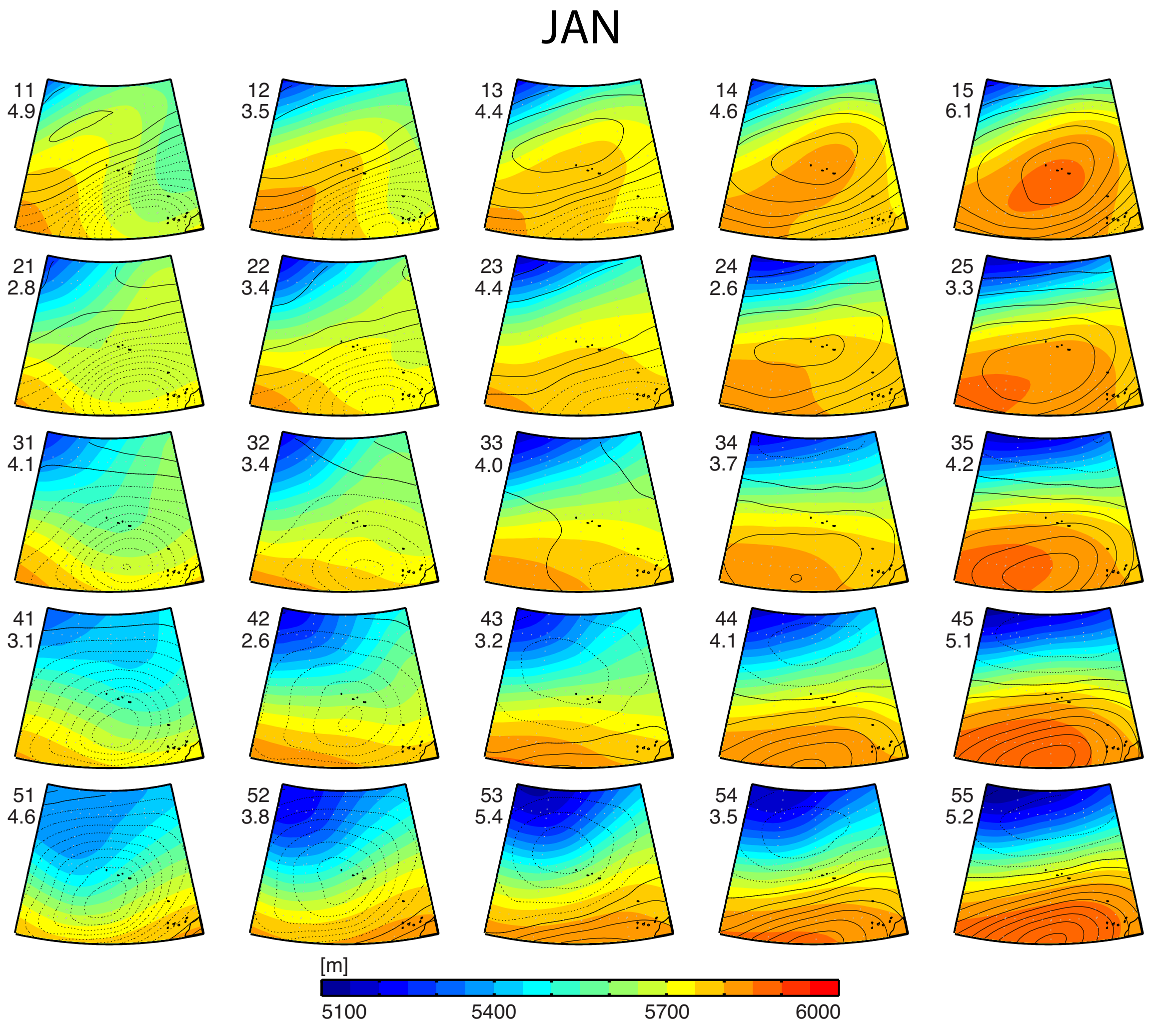

Pre-trough: 43, 52, 53, 54, 55
Trough: 21, 31, 41, 42, 51
Post-trough: 11, 12
Ridge: 13, 14, 15, 23, 24, 25
Zonal: 34, 35, 44, 45
Unclassified: 22, 32, 33

Figure S1: SOM nodes of 500-mb geopotential heights with overlaid contours of normalized 500-mb geopotential height anomalies for January. These monthly-window nodes are calculated from the anomalies obtained from mean and standard deviation values taken over 31-day centered windows. The numbers in the upper left-hand portion of each node indicate node number in matrix notation, and the relative frequency of occurrence of each node. Each of the 25 nodes is classified into different synoptic categories, as described in the manuscript.

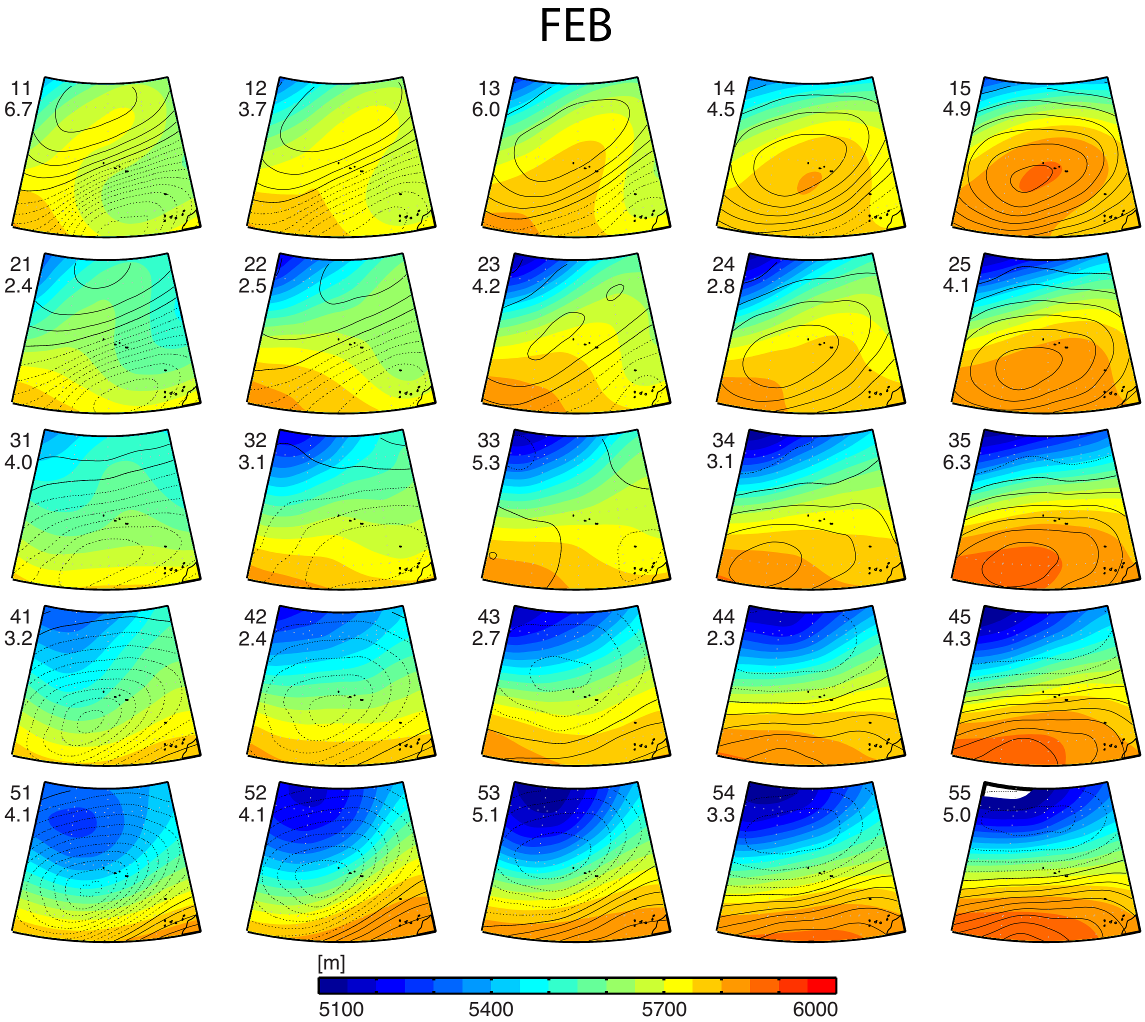

Pre-trough: 33, 44, 54
Trough: 41, 42, 43, 51, 52, 53
Post-trough: 11, 12, 21, 22, 32
Ridge: 13, 14, 15, 23, 24, 25
Zonal: 35, 45, 55
Unclassified: 31, 34

Figure S2: As in Fig. S1 but for February.

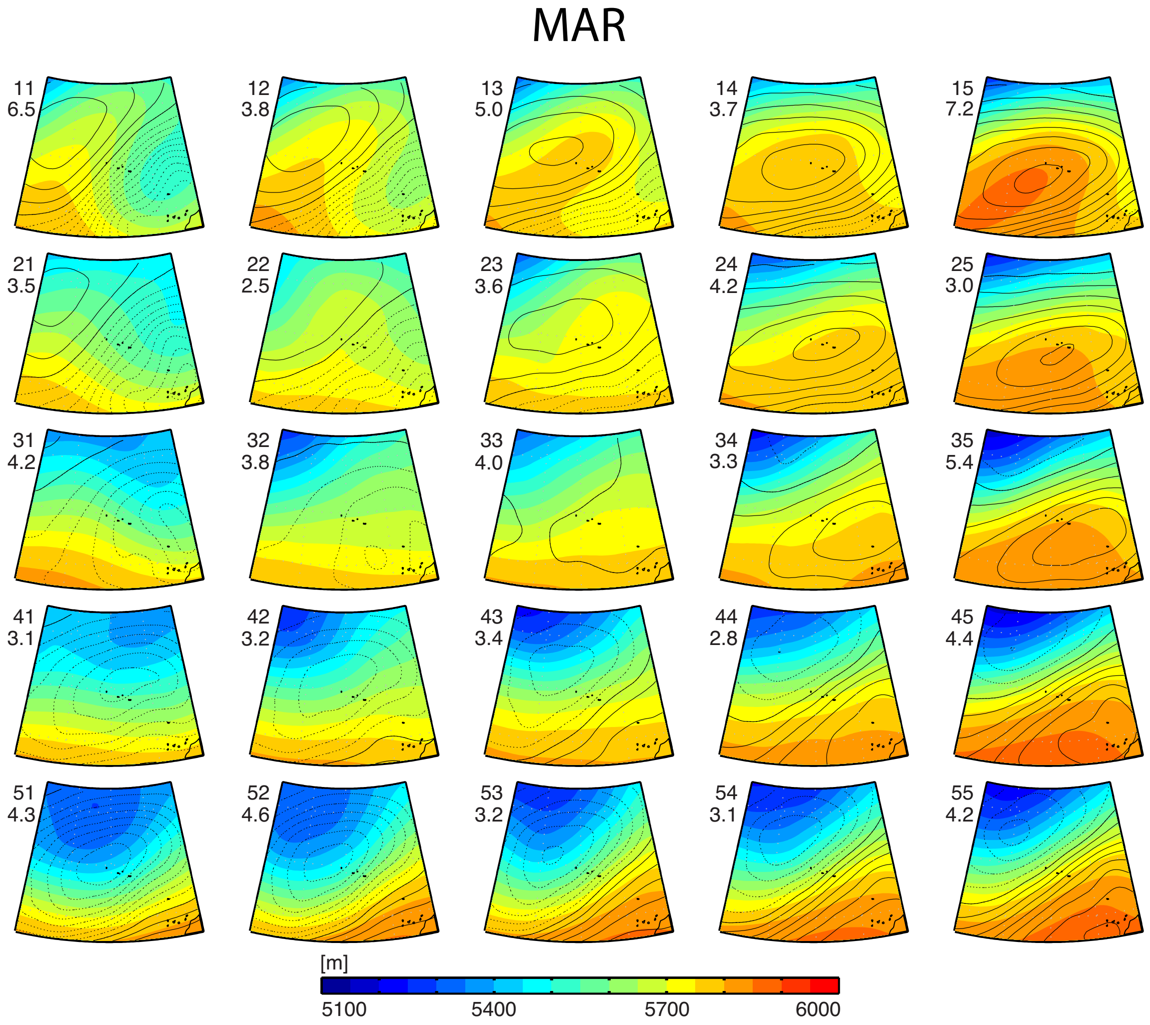

Pre-trough: 44, 45, 54, 55
Trough: 41, 42, 43, 51, 52, 53
Post-trough: 11, 12, 21, 31
Ridge: 13, 14, 15, 22, 23, 24, 25, 35
Zonal: —
Unclassified: 32, 33, 34

Figure S3: As in Fig. S1 but for March.

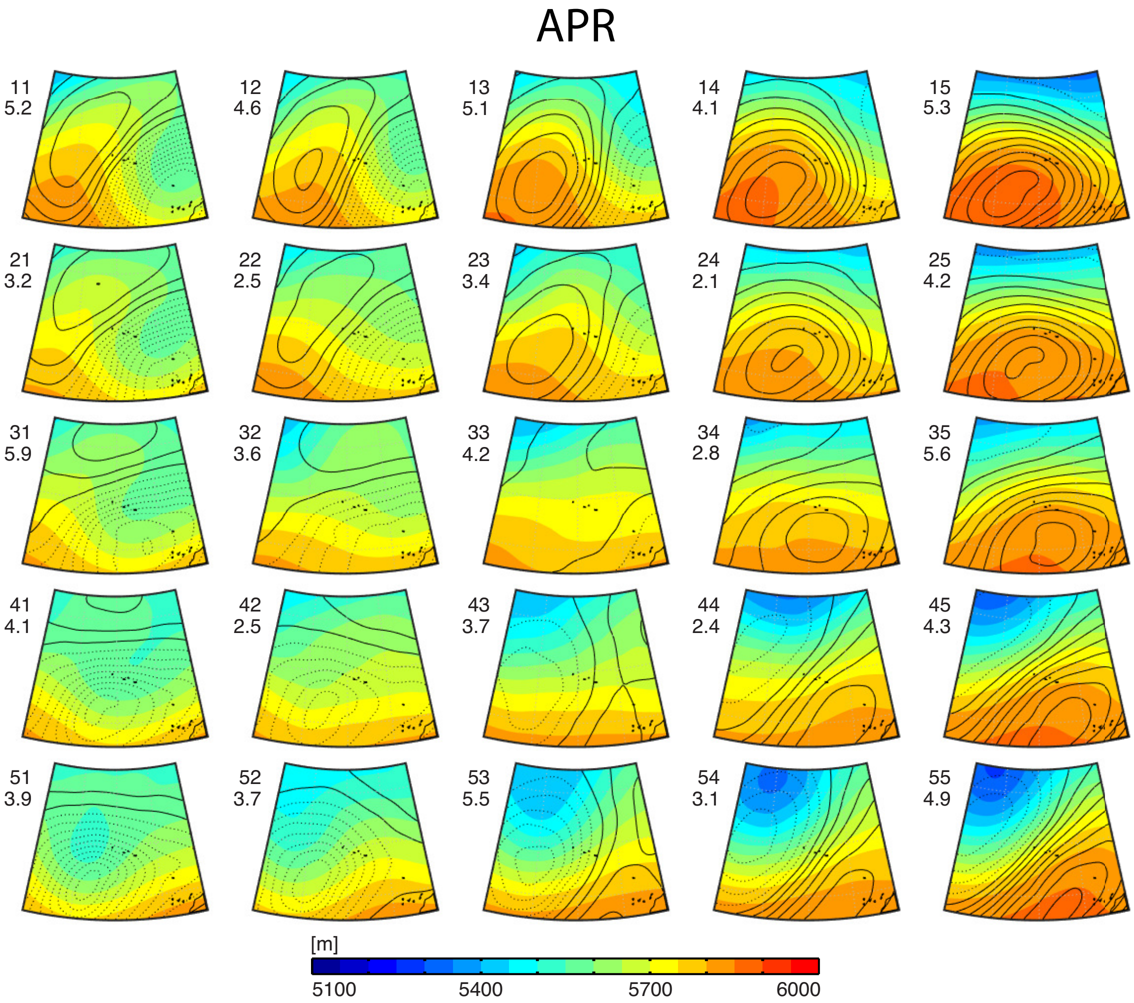

Pre-trough: 42, 45, 52, 53, 54, 55
Trough: 31, 41, 51
Post-trough: 11, 12, 13, 21, 22
Ridge: 14, 15, 23, 24, 25, 35
Zonal: 33, 34, 43, 44
Unclassified: 32

Figure S4: As in Fig. S1 but for April.

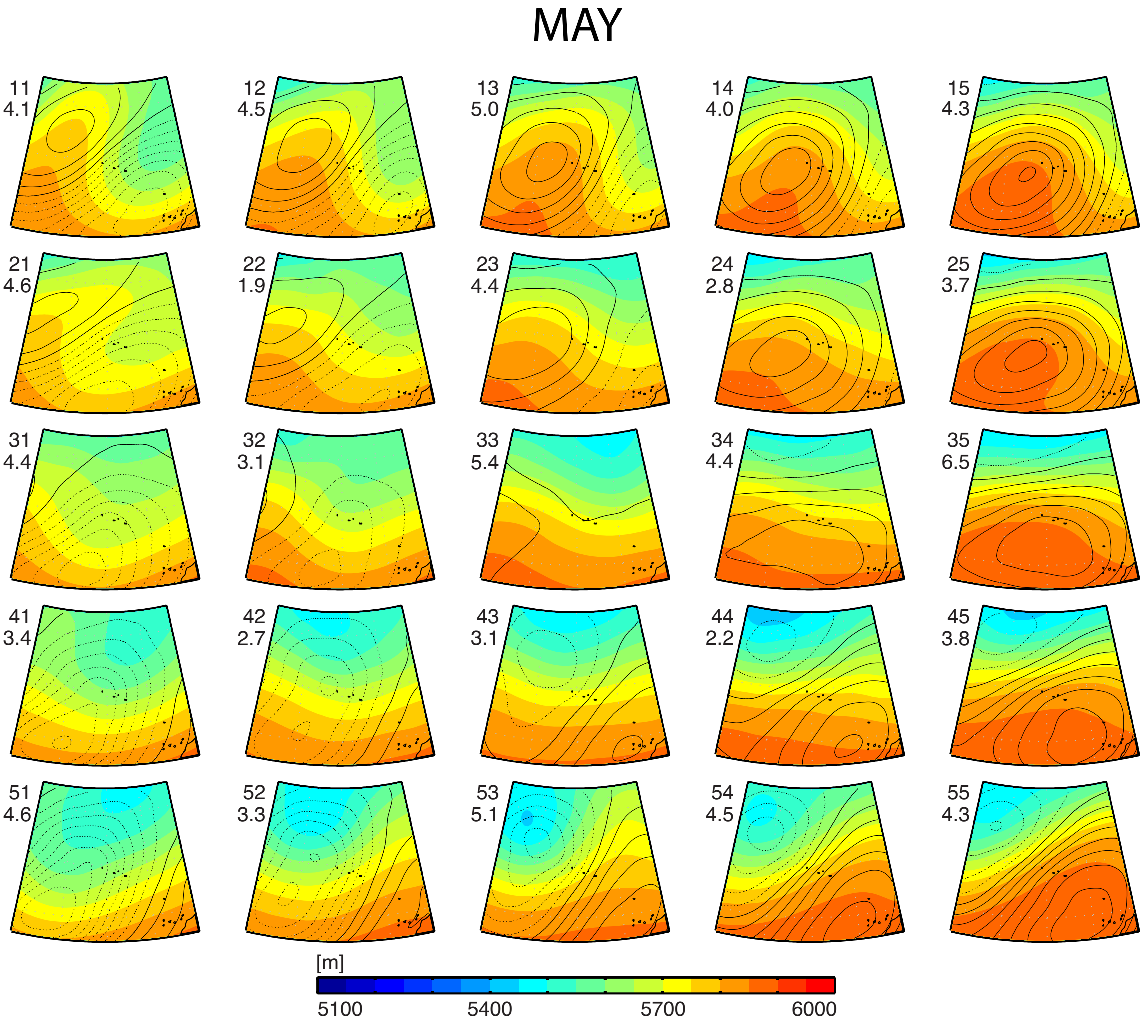

Pre-trough: 45, 53, 54, 55
Trough: 31, 32, 33, 41, 42, 43, 51, 52
Post-trough: 11, 12, 13, 21, 22, 23
Ridge: 14, 15, 24, 25, 35
Zonal: 34, 44
Unclassified: —

Figure S5: As in Fig. S1 but for May.

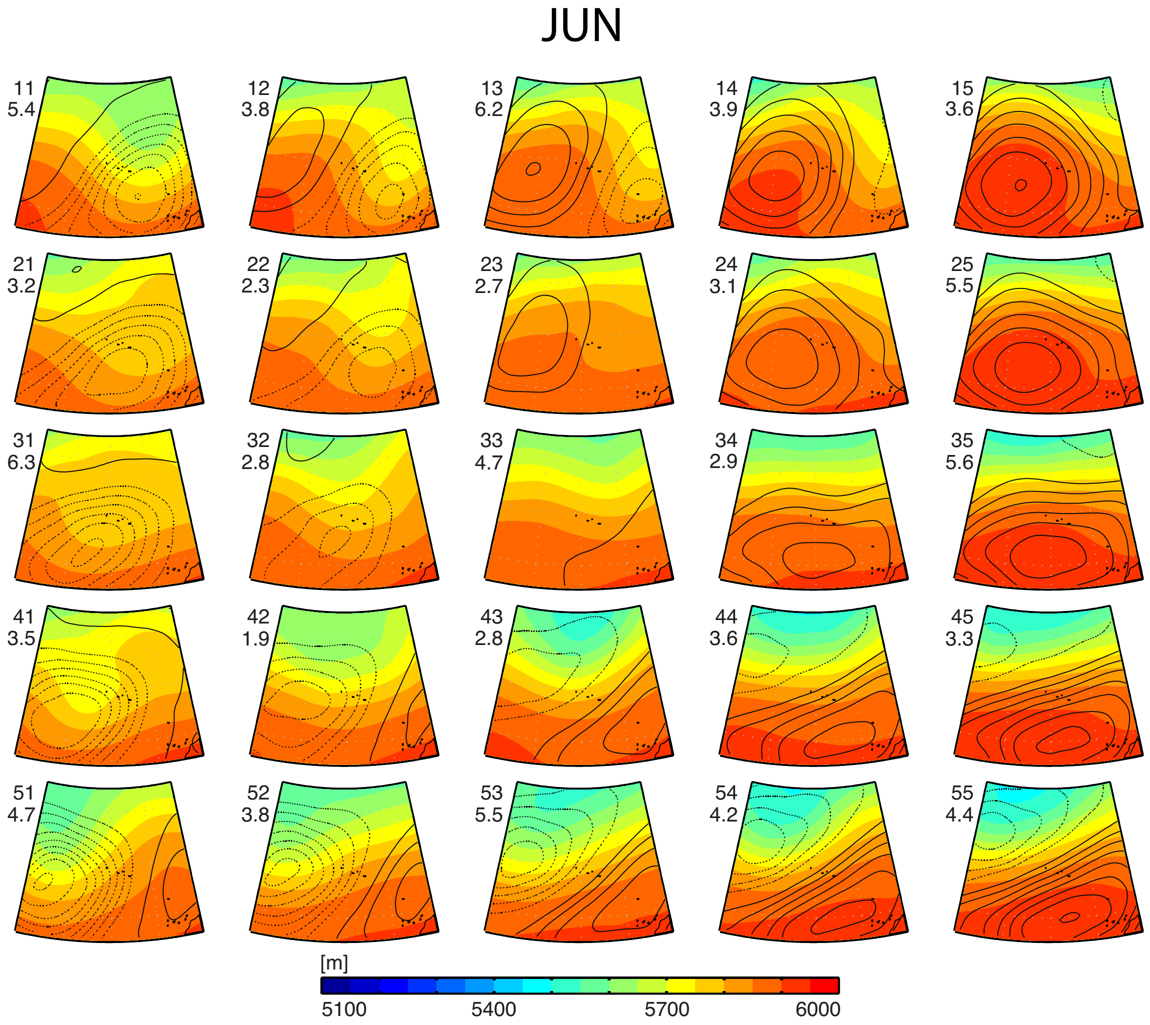

Pre-trough: 51, 52, 53, 54, 55
Trough: 21, 31, 32, 41, 42, 43
Post-trough: 11, 12, 13, 22, 23, 33
Ridge: 14, 15, 24, 25, 35
Zonal: 34, 44
Unclassified: —

Figure S6: As in Fig. S1 but for June.

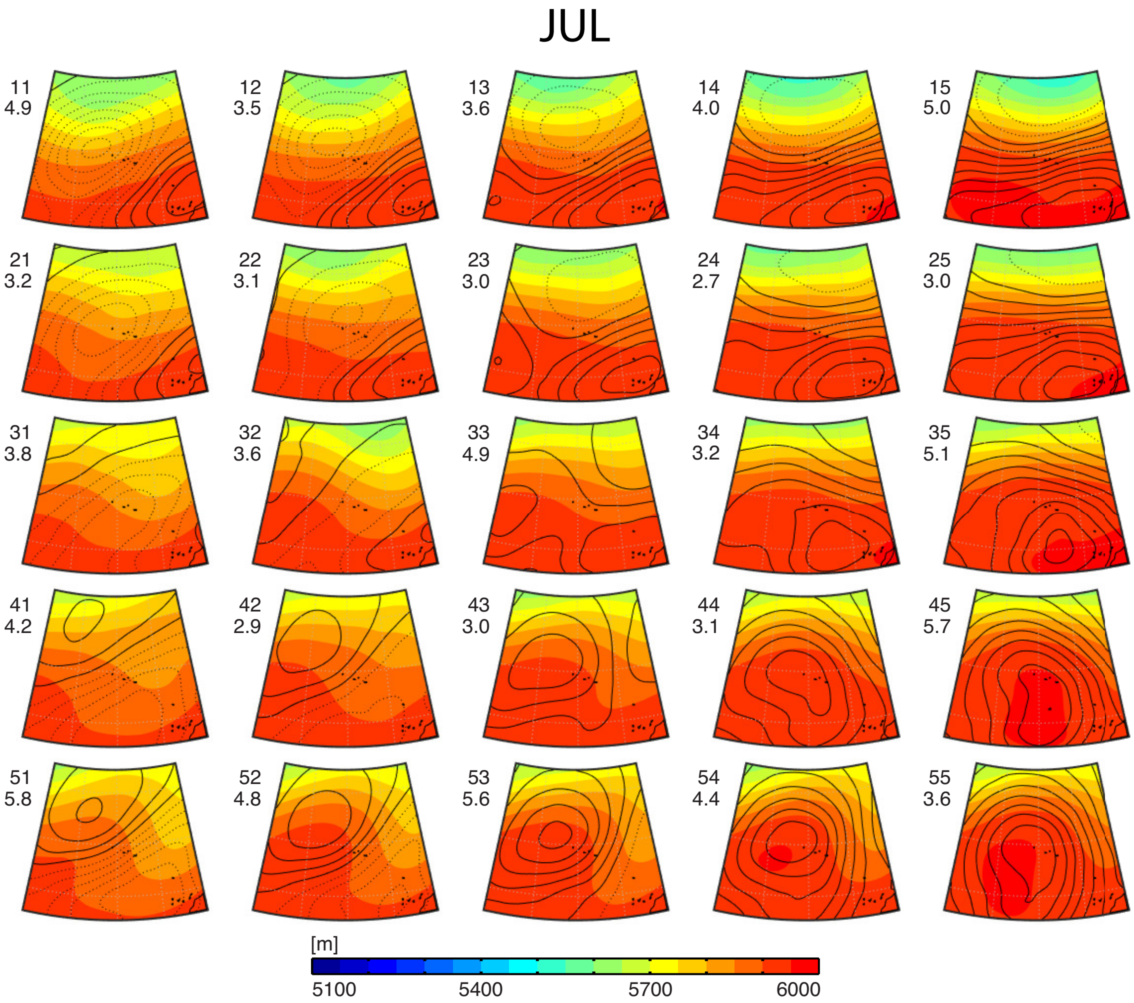

Pre-trough: —
Trough: 11, 12, 13, 14, 15, 21, 22, 23
Post-trough: 31, 32, 33, 41, 42, 43, 51, 52, 53
Ridge: 44, 45, 54, 55
Zonal: 24, 25, 34, 35
Unclassified: —

Figure S7: As in Fig. S1 but for July.

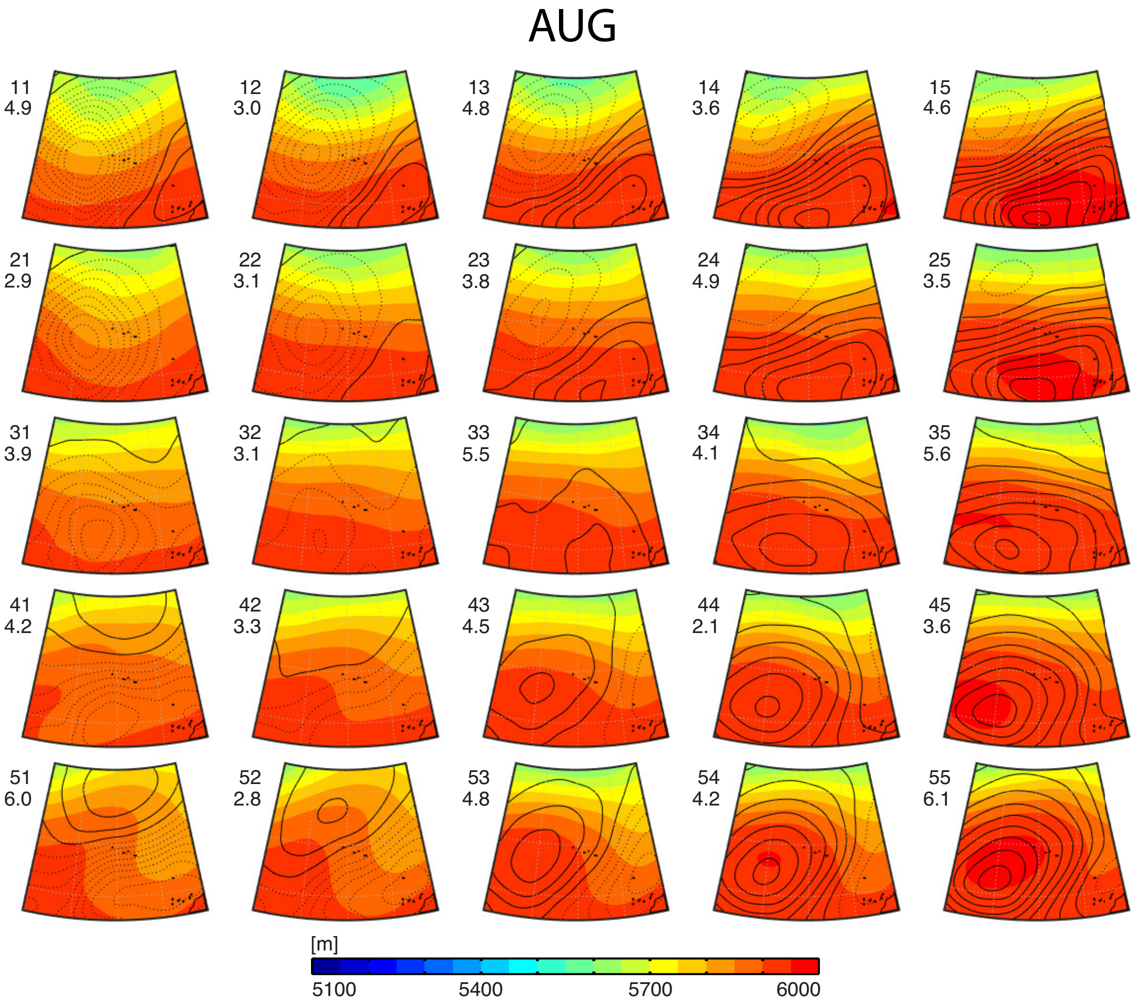

Pre-trough: 14, 15
Trough: 11, 12, 13, 21, 22, 31
Post-trough: 33, 34, 42, 51, 52, 53
Ridge: 35, 43, 44, 45, 54, 55
Zonal: 23, 24, 25
Unclassified: 32, 41

Figure S8: As in Fig. S1 but for August.

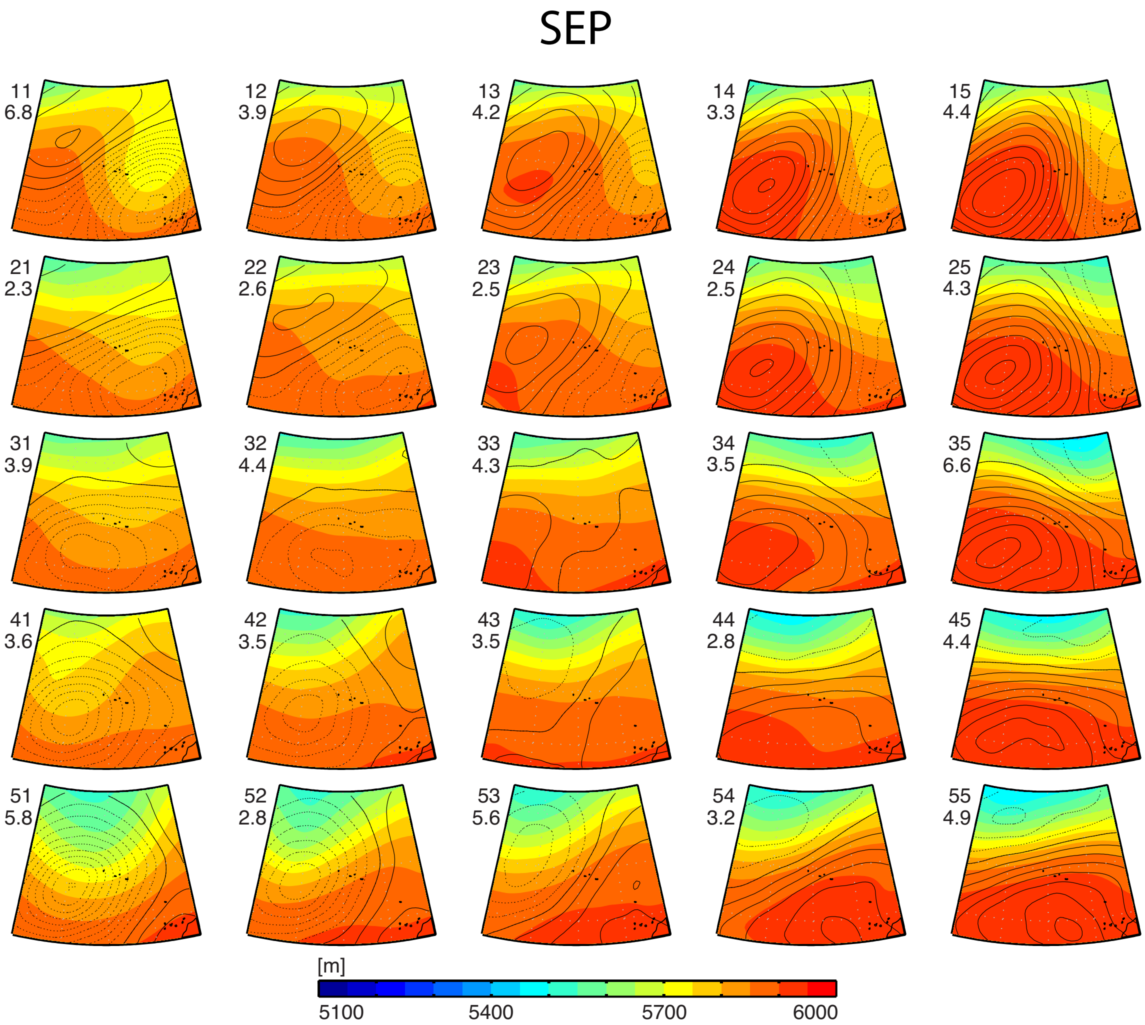

Pre-trough: 52, 53, 54
Trough: 21, 22, 31, 32, 42, 43, 51
Post-trough: 11, 12, 13, 14
Ridge: 15, 23, 24, 25, 35
Zonal: 33, 34, 44, 45, 55
Unclassified: 41

Figure S9: As in Fig. S1 but for September.

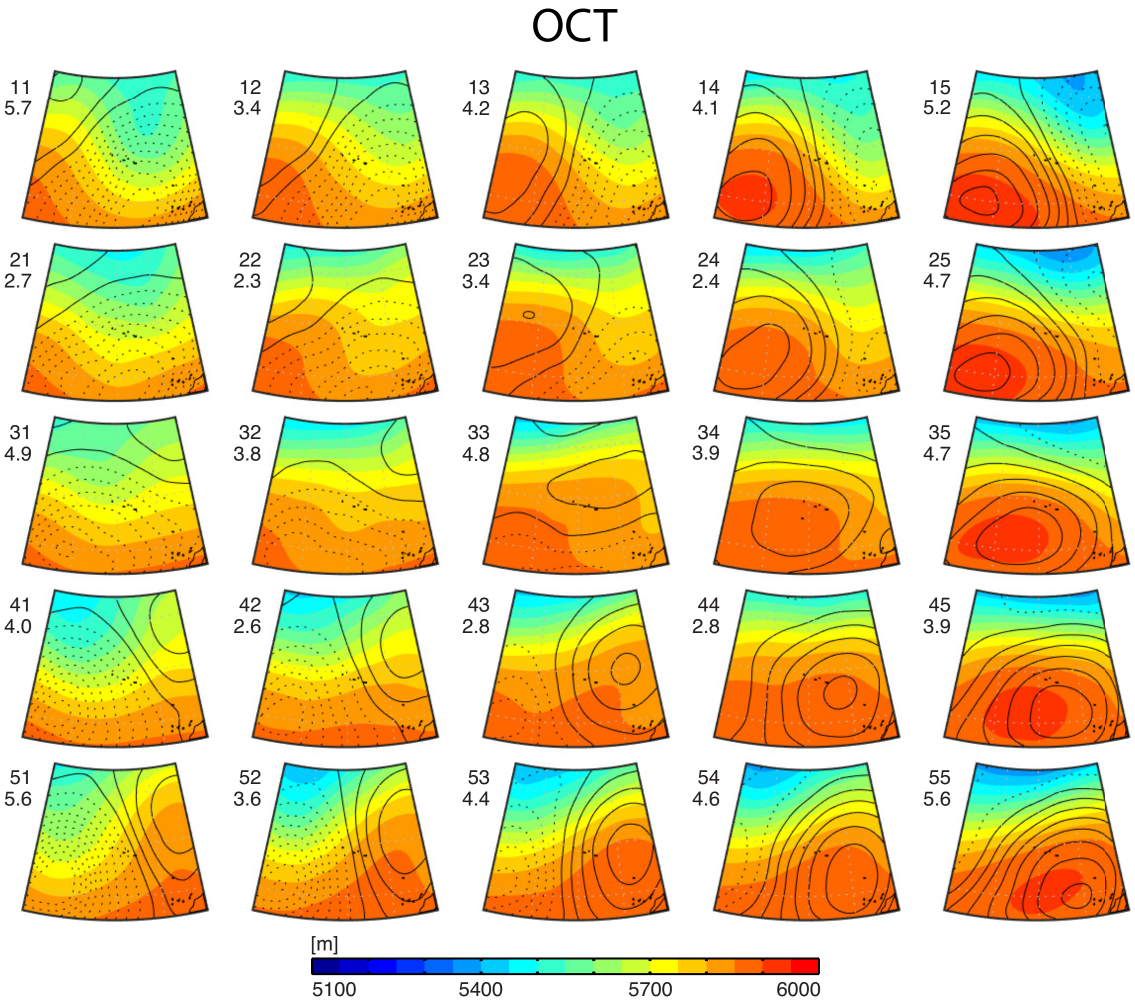

Pre-trough: 42, 43, 51, 52, 53, 54
Trough: 21, 22, 31, 32, 41
Post-trough: 11, 12, 13, 14, 15, 23, 24, 25
Ridge: 34, 35, 45, 55
Zonal: 44
Unclassified: 33

Figure S10: As in Fig. S1 but for October.

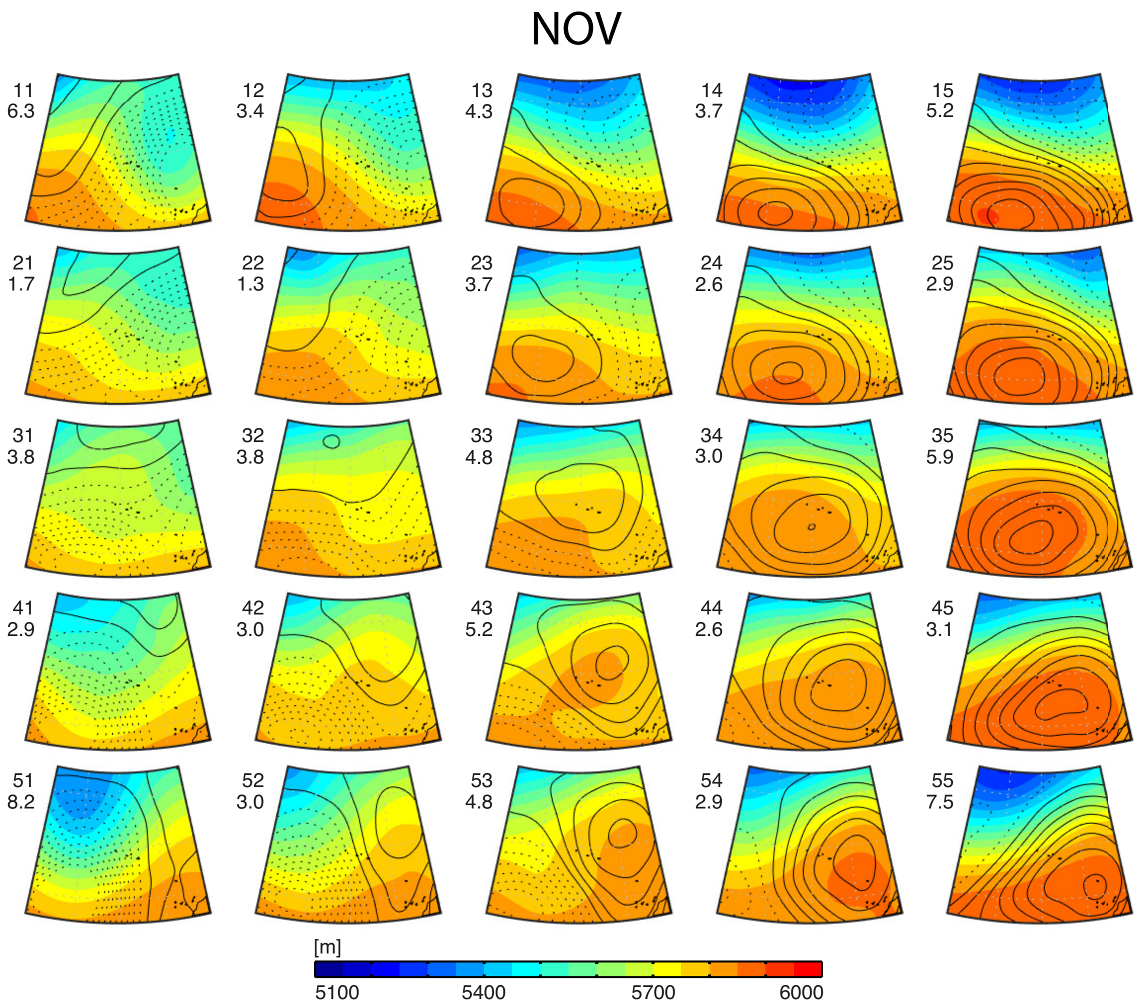

Pre-trough: 42, 44, 52, 53, 54, 55
Trough: 31, 41, 51
Post-trough: 11, 12, 13, 14, 15, 21
Ridge: 24, 25, 33, 34, 35, 43, 45
Zonal: 23
Unclassified: 22, 32

Figure S11: As in Fig. S1 but for November.

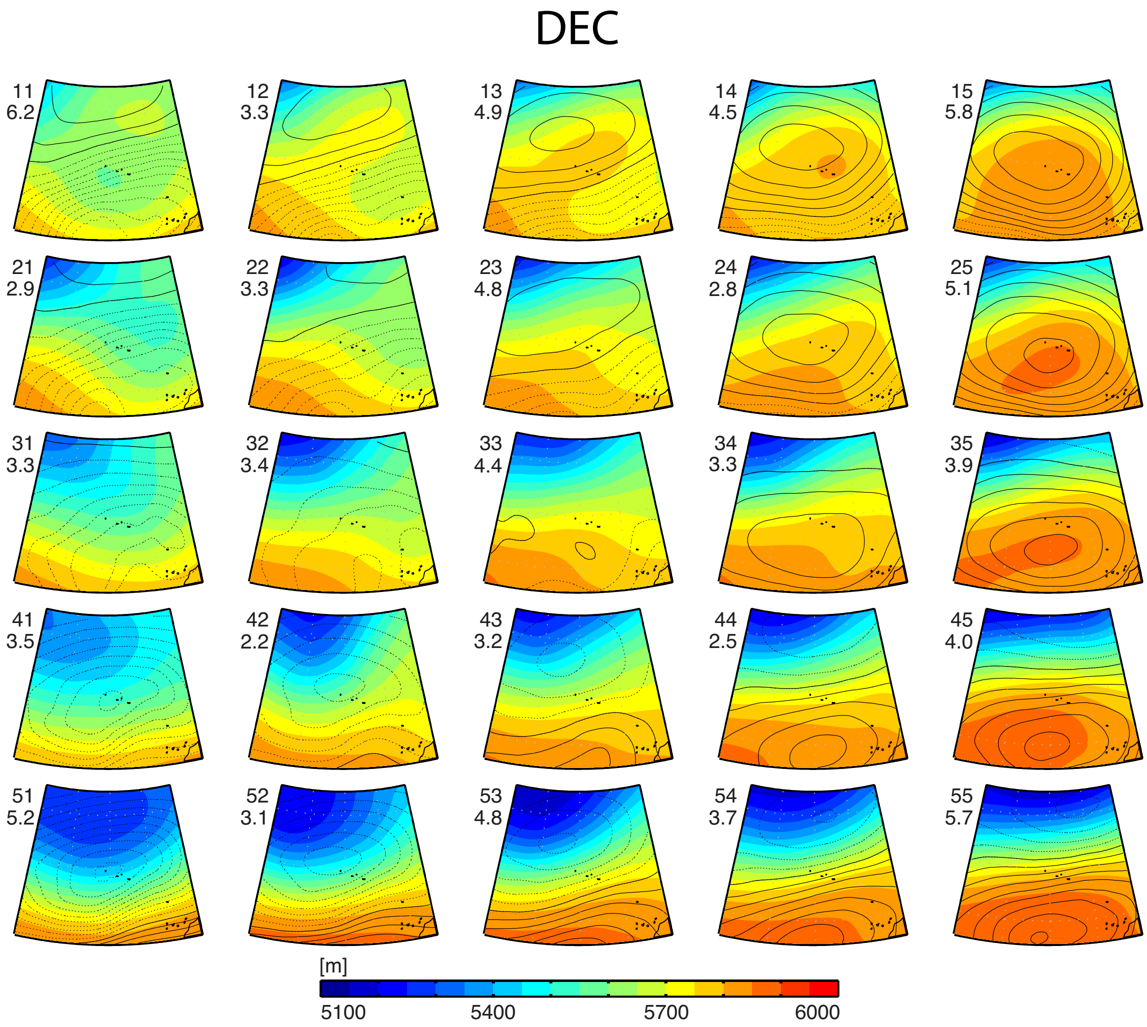

Pre-trough: 43, 53, 54
Trough: 11, 21, 31, 41, 42, 51, 52
Post-trough: 12, 22, 32
Ridge: 13, 14, 15, 23, 24, 25
Zonal: 44, 45, 55
Unclassified: 33, 34, 35

Figure S12: As in Fig. S1 but for December.

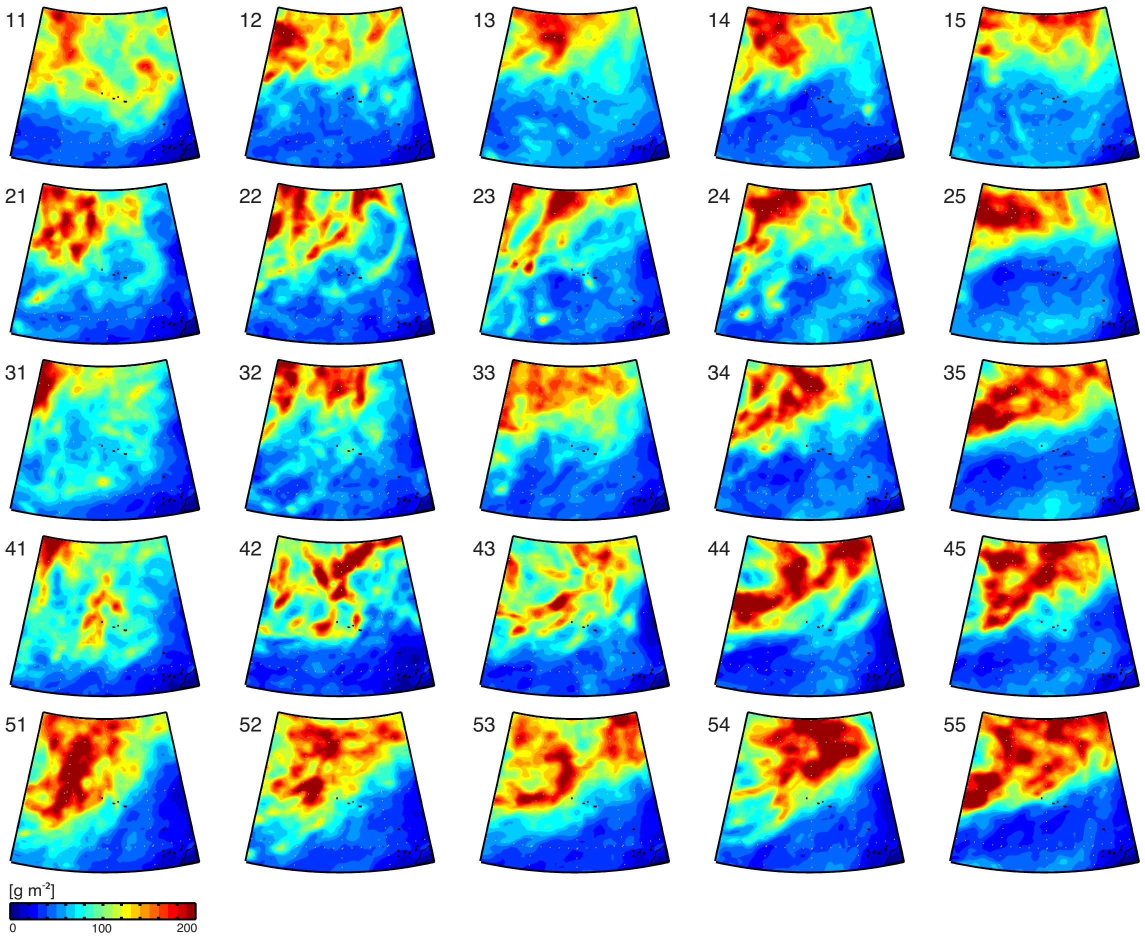

Figure S13: Mean column-total condensate from ERA–Interim for each SOM node for June. Nodes 53, 31, 13, and 35 correspond to the four archetypal ~~synotpic~~ regimes shown in Fig. 7